Supporting Information

Catenated Imide-linked Porous Organic Polymer for Solar Energy Harvesting

*Morteza Torabi,†[a] Iman M. Imani,†[b] Seung-Bum Kim,[b,c] Sunghoon Hur,[c] Hyun-Cheol Song,[b] Mohammad Ali Zolfigol[d] and Saeid Azizian[a]**

[a] *Department of Physical Chemistry, Faculty of Chemistry and Petroleum Sciences, Bu-Ali Sina University, Hamedan, Iran*

[b] *Department of Materials Science and Engineering, Korea University, Seoul 02841, Republic of Korea*

[c] *Electronic Materials Research Center, Korea Institute of Science and Technology (KIST), Seoul 02792, Republic of Korea*

[d] *Department of Organic Chemistry, Faculty of Chemistry and Petroleum Sciences, Bu-Ali Sina University, Hamedan, Iran*

Correspondence to: S. Azizian, Email: sazizian@basu.ac.ir

Table of contents:

1. List of figures and tables:

Figure S14: Surface temperature increasing results of dry catenated Co-abpy-POP (a) and Ligand-2 (b) under sunlight illumination during 600 s, the Infrared images of catenated Co-abpy-POP (c), and Ligand-2 (d) under the aforementioned conditions.

Figure S15: Mass change and evaporation rate of Ligand-2 (a) and catenated Co-abpy-POP (b) under sunlight irradiation.

Figure S16: Photos of the wettability of catenated Co-abpy-POP and Ligand-2.

Figure S17: Conductivity increase of aqueous solution of ISSG setup over time under dark conditions due to dissolution of formed salt crystals on the sample surface.

Figure S18: Water mass change and evaporation rate of catenated Co-abpy-POP for distilled water (a), 3% NaCl concentration (b), 10% NaCl concentration (c).

Figure S19: Investigating the stability of the evaporation rate of water using the catenated Co-abpy-POP system during 480 min (a), water mass change by the catenated Co-abpy-POP absorber under 1.0 sun irradiation during 8 h light irradiation (b).

Figure S20: Mass change and evaporation rate of water using a 10% NaCl solution in the presence of catenated Co-abpy-POP for five cycles of 10 h continuous desalination.

Figure S21: The images of the anti-salt fouling potential of catenated Co-abpy-POP for five cycles of 10 h continuous desalination and 1 h darkness condition.

Figure S22: The image of the catenated Co-abpy-POP-based system used for photothermal water desalination and removal of methyl orange (a), the images of the condenser system containing catenated Co-abpy-POP-based solar steam generation and water collection, before (b) and after (c) sunlight irradiation.

Figure S23: The diagram of collected water over time for catenated Co-abpy-POP-based solar water desalination.

Figure S24: Schematic illustration of evaporator under varying sunlight angles (forenoon, noon, and afternoon), demonstrating stable photothermal performance of catenated Co-abpy-POP-

based system throughout the day. Infrared thermal images showing surface heating under different illumination conditions. The plotted data compares water mass change over time for the catenated Co-abpy-POP-based system versus control setups, highlighting its enhanced evaporation capability.

Figure S25: Mass change and evaporation rate of catenated Co-abpy-POP decorated on cotton fabric by using calcium alginate hydrogel as binder.

Figure S26: The confirmation of adherence stability of catenated Co-abpy-POP coated on cotton fabric using calcium alginate binder during washing by the water stream.

Figure S27: (A) N_2 adsorption–desorption isotherms and (B) pore size distribution of abpy-POP

Figure S28: XRD pattern of abpy-POP, indicating its amorphous structure

Figure S29: Surface temperature increasing curve of dry abpy-POP under 1.0 sun illumination during 600 s

Figure S30: Mass change and evaporation rate of abpy-POP under 1.0 sun irradiation

Figure S31: (a) XPS survey spectrum of Co-abpy-POP showing peaks for C, N, O, Co, and Cl. (b) High-resolution C(1s) XPS spectrum peaks. (c) High-resolution N(1s) XPS spectrum peaks. (d) High-resolution O(1s) XPS spectrum peak. (e) High-resolution Co(2p) XPS spectrum displaying Co(II)($2p_{3/2}$), Co(III)($2p_{3/2}$), Co(II)($2p_{1/2}$), and Co(III)($2p_{1/2}$) peaks. (e) High-resolution Cl(2p) XPS spectrum showing Cl($2p_{3/2}$) and Cl($2p_{1/2}$) peaks.

Figure S32: The E% of the Co-abpy-POP-based nanofluids with different concentrations (0.01, 0.02, and 0.04 g per 6 mg PEG) and pure PEG solution versus temperature.

Figure 33: (A) Mass change and evaporation rate of water in Co-abpy-POP-based hybrid ISSG+PTE, (B) the output voltage, (C) output current and (D) output power density of Co-abpy-POP-based hybrid ISSG+PTE

Table S1: Comparison of the performance of Co-abpy-POP upon the solar steam generation by the previously reported systems under 1.0 sun irradiation.

Table S2: Comparison of performance of Co-abpy-POP and some of reported materials in DASC

Table 3: Comparison of the output power density of Co-abpy-POP with some of reported PTE systems

2. Supplementary Note 1. Materials and methods

All reagents and starting materials in this research were commercially provided from Merck and Sigma-Aldrich companies and used without further treatment. FT-IR spectra were carried out with FT-IR spectrometer, PerkinElmer Spectrum 65 model. ^{1}H NMR and ^{13}C NMR spectra were recorded on a Bruker spectrometer operating at 250 and 62 MHz, respectively, and a high-resolution solid-state NMR spectrum (600 MHz, 14. 1T, triple resonance, wide bore) was used to characterize the chemical structure of catenated Co-abpy-POP. Chemical shifts are given in ppm relative to TMS. Field emission scanning electron microscopy (FESEM) analysis was conducted by the TESCAN MIRA4 instrument with an energy-dispersive X-ray spectroscopy (EDS) and elemental detector. High-resolution transmission electron microscopy (HR-TEM) analysis was performed on a Titan G2 Cube 60-300. X-ray diffraction (XRD) data were recorded on a X'Pert Pro instrument. Nitrogen adsorption/desorption isotherms were measured on a BELSORP Mini adsorption analyzer. Thermal gravimetric analysis (TGA) was carried out on a Sanaf, TGA-1000 model. X-ray photoelectron spectroscopy (XPS) was conducted on a Bes Tek spectrometer equipped with an Al-Kα X-ray source ($h\upsilon$ = 1486.6 eV). Electron paramagnetic resonance (EPR) measurement was recorded at room temperature using an EPR200M spectrometer from CIQTEK Company. The UV–visible spectrophotometry was measured on a PG-Instrument-T80 spectrophotometer at room temperature, and diffuse reflectance spectroscopy (DRS) was carried out by Shimadzu UV-2600 model. Solar simulator (using xenon lamp, CERMAX 300 W) was used in photothermal experiments. Infrared thermal imaging camera (Hti HT-18) was applied to record the surface temperature of solar absorbers in dry and wet states. A thermoelectric generator, TEG (TEG-12708T23740 40 mm model), was used for photo-thermoelectric conversion tests. The mass change of the system was recorded with an analytical balance (METTLER TOLEDO, J81603-C/ FACT), ± 0.0001 g. The digital multimeter data logger (PROVA 803) was applied to record the output voltage.

3. Supplementary Note 2. Experimental section

3.1. Photothermal conversion and steam generation capacity experiments

Photo-thermal and photo-thermoelectric conversion was performed under direct illumination of a solar simulator. The solar absorber system for seawater desalination consists of a glass beaker containing bulk water, and its surface is wrapped with cotton fabric around insulating foam to

minimize heat loss. Because of the superhydrophilic nature of Ligand-2 and catenated Co-abpy-POP powders, in the wet state of each sample sticks together and adheres to the surface of cotton fabric without using any binder. However, the role of binder was also investigated, and calcium alginate hydrogel was used as a binder to enhance the physical stability of the system during water transport and mechanical washing. The surface temperature of Ligand-2 and catenated Co-abpy-POP is recorded using an infrared thermal imaging camera (Hti HT-18). The mass change of water was measured using an analytical balance (METTLER TOLEDO, J81603-C/ FACT), and the data were recorded every 30 s by using a data acquisition system connected to a PC. In the photo-thermoelectric device, a thin layer of solar absorber was fixed on the surface of a thermo-electric generator (TEG), and silicon oil was used as a binder. The sample was directly exposed to light illumination, while the other side of the TEG was connected to a heat sink. The output voltage of the system was monitored using a digital multimeter data logger (PROVA 803 model). For nanofluid-based DASC works, a cylindrical glass was filled with PEG-400, and certain amounts of the solar absorber were dispersed in PEG-400 by an ultrasonic homogenizer to have a stable colloidal system, then the temperature of the system was monitored at different time intervals during light illumination.

3.2. Synthesis of 2,6-bis(1*H*-benzo[*d*]imidazol-2-yl)pyridine

The required precursors were synthesized according to our recently reported educational synthetic organic theory.[1]

2,6-bis(1*H*-benzo[*d*]imidazol-2-yl)pyridine was synthesized according to the reported procedure.[2] 2,6-pyridine dicarboxylic acid (6 mmol, 1 g) and 1,2-phenylendiamine (13 mmol, 1.4 g), and orthophosphoric acid (20 mL) were added to a 25 mL round-bottomed flask and heated for 4 h at 220 °C. After that, the hot solution was poured into cold distilled water (100 mL) and stirred vigorously. The resulting precipitate was filtered and washed with water. Then, the solid was dispersed in 100 mL solution of $NaHCO_3$ (10 % w/v), collected by filtration, and washed with cold MeOH (100 mL) to yield pure product (Yield= 85%).

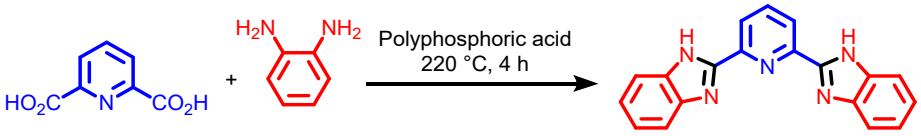

Scheme S1: Schematic synthesis of 2,6-bis(1*H*-benzo[*d*]imidazol-2-yl)pyridine.

3.3. Synthesis of 2,6-bis(5-nitro-1*H*-benzo[*d*]imidazol-2-yl)pyridine

Initially, 2,6-bis(1*H*-benzoimidazol-2-yl)pyridine (9 mmol, 2.8 g) was added to a 25 mL round-bottomed flask, and 15 mL of concentrated sulfuric acid was poured into it. Next, 2 mL of concentrated nitric acid at 0 °C was added dropwise to the reaction mixture, and the reaction was continued for 4 h at room temperature to complete the nitration reaction. Next, the reaction mixture was poured into 100 mL of ice-water mixture, and the precipitate was collected using filtration and neutralized by $NaHCO_3$ solution (10 % w/v) and washed several times with cold water to obtain the desired product (Yield = 80%).

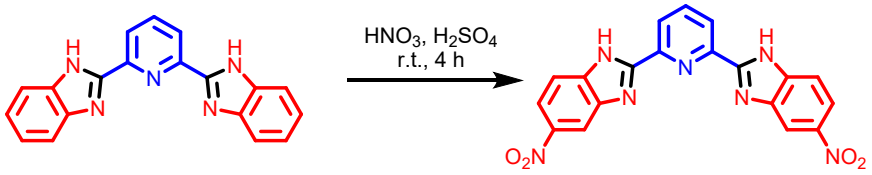

Scheme S2: Illustration of the synthesis of 2,6-bis(5-nitro-1*H*-benzo[*d*]imidazol-2-yl)pyridine.

3.4. Synthesis of 2,2'-(pyridine-2,6-diyl)bis(1*H*-benzo[*d*]imidazol-5-amine) (Ligand-1)

First, $SnCl_2.2H_2O$ (20 mmol, 4.72 g) was dissolved in 10 mL of concentrated hydrochloric acid. In another glass, 2,6-bis(5-nitro-1*H*-benzo[*d*]imidazol-2-yl)pyridine (2.5 mmol, 1 g) was dissolved in 20 mL of hot acetic acid and added to the acidic solution of $SnCl_2.2H_2O$ dropwise, and the reaction mixture was heated at 100 °C for 12 h. After the completion of the reaction, the solvent was removed and the remaining solid was neutralized with $NaHCO_3$ solution (10 % w/v),

collected by filtration, and washed several times with water and then EtOH (10 mL) to yield Ligand-1 (Yield= 55%).

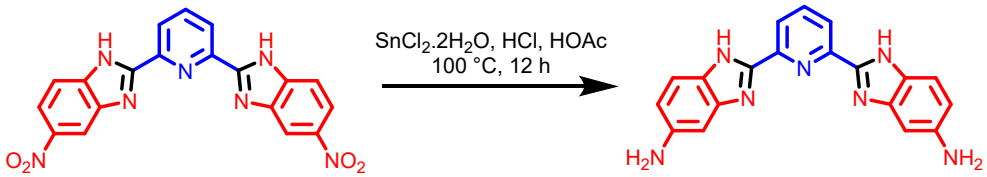

Scheme S3: General procedure for the synthesis of Ligand-1.

3.5. Synthesis of Ligand-2

Ligand-2 was synthesized based on previous reports.[3] 0.2 mmol (0.068 g) of Ligand-1 was dissolved in 20 mL of MeOH. Besides, 0.1 mmol (0.023 g) of $CoCl_2.6H_2O$ was dissolved in 5 mL of MeOH and added to Ligand-1 solution. The reaction mixture was then refluxed at 60 °C for 24 h. After completion of the reaction, the solvent was removed, and the remaining precipitate was washed with 40 mL of diethyl ether and then 10 mL EtOH and dried at 80 °C (Yield = 75 %).

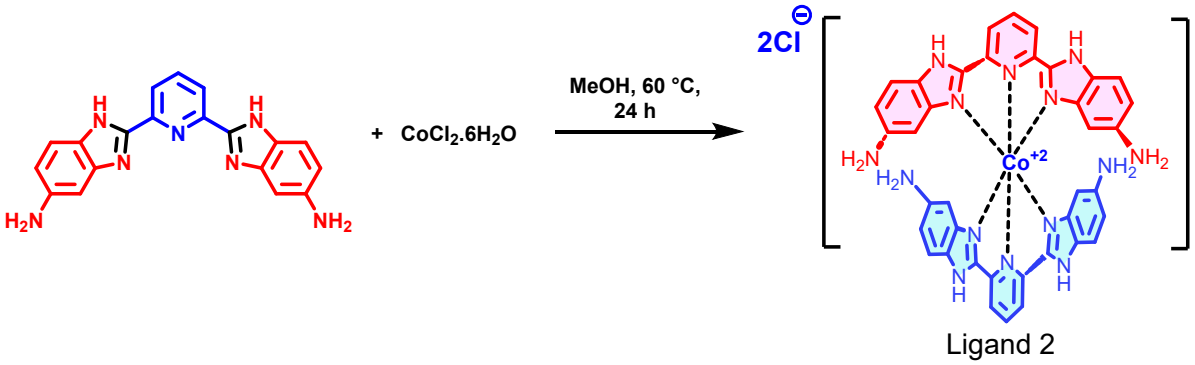

Scheme S4: Synthesis of Ligand-2.

3.6. Synthesis of catenated Co-abpy-POP

Initially, a mixture of Ligand-2 (0.5 mmol, 0.406 g), perylene tetracarboxylic dianhydride (PTA) (0.6 mmol, 0.235 g), 0.1 g of $Zn(OAc)_2$ as a catalyst, and 5 g of imidazole was added to a 25 ml flask and heated at 160 °C for 72 h under an inert atmosphere. After that, the reaction mixture was cooled, and the precipitate was washed with MeOH, diluted HCl solution, and THF separately to remove unreacted starting materials, imidazole, and $Zn(OAc)_2$, then dried at 80 °C for 12 h (Yield = 50%).

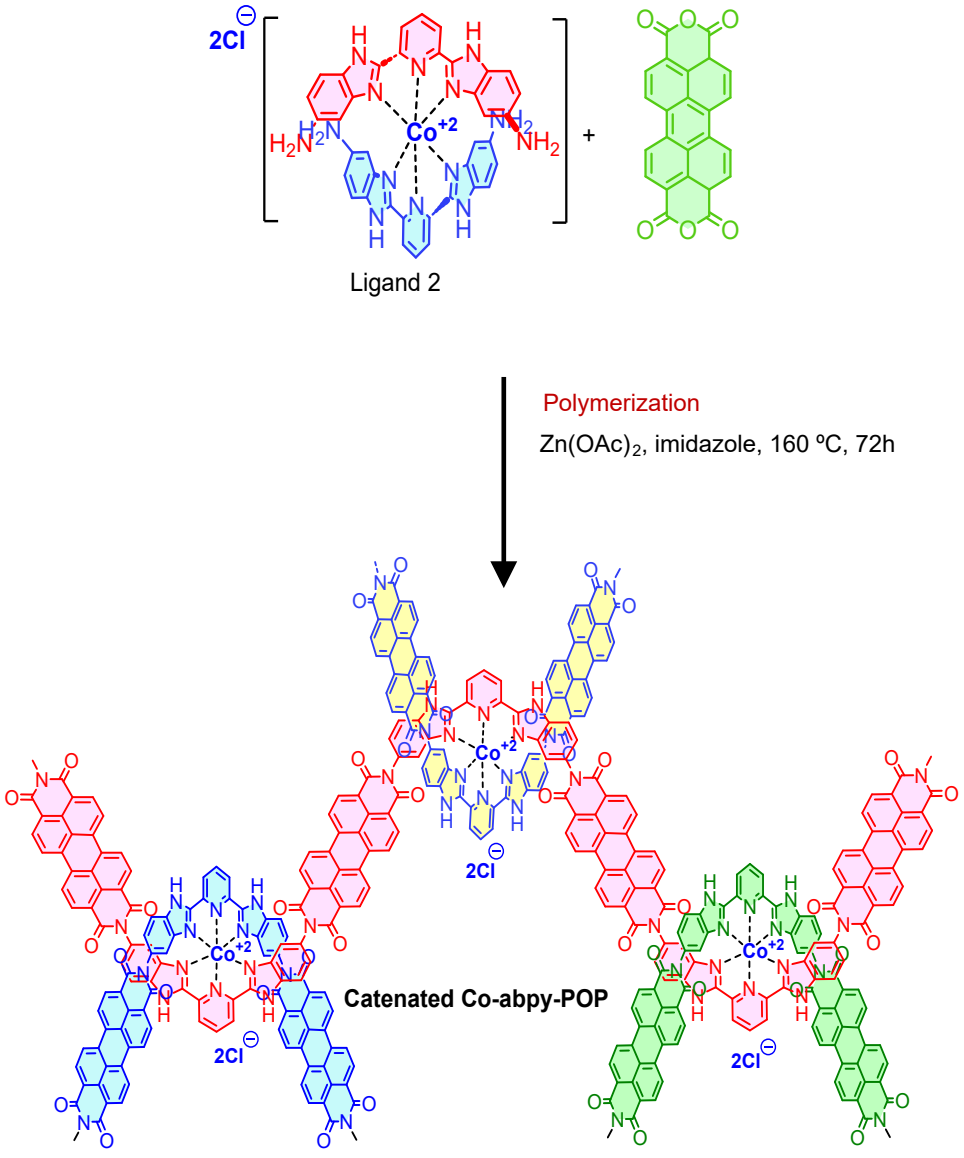

Scheme S5: Synthesis of catenated Co-abpy-POP.

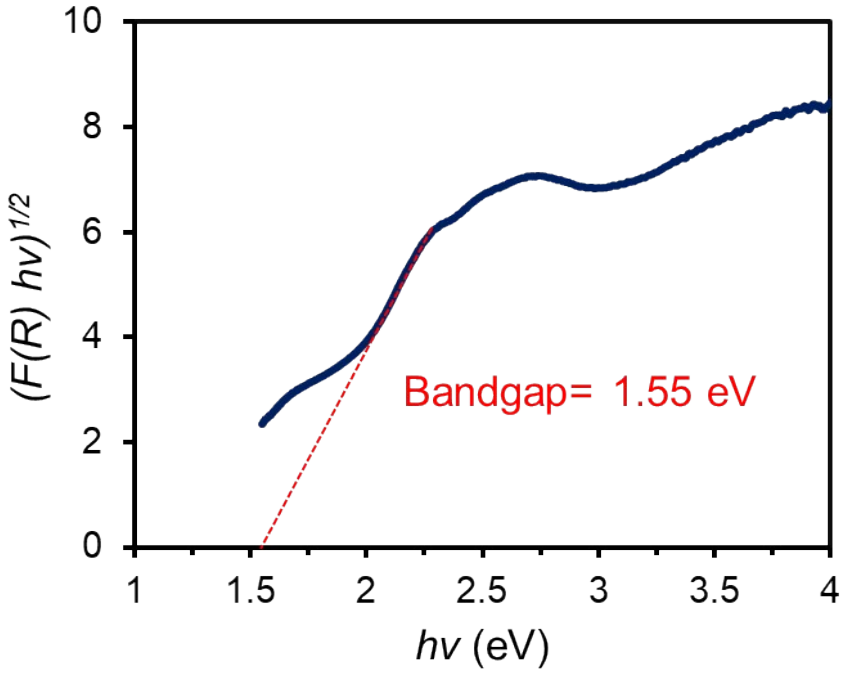

Figure S1: Bandgap determination for Co-abpy-POP.

4. Characterization section

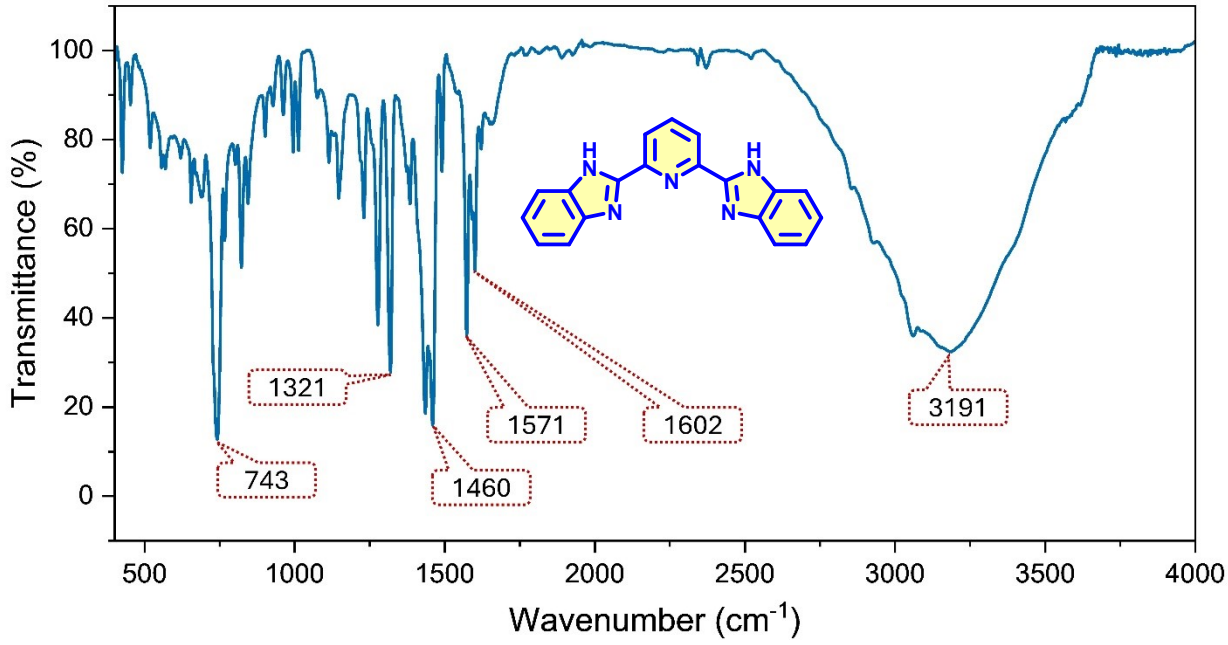

Figure S2: FT-IR spectrum of 2,6-bis(1*H*-benzo[*d*]imidazol-2-yl)pyridine.

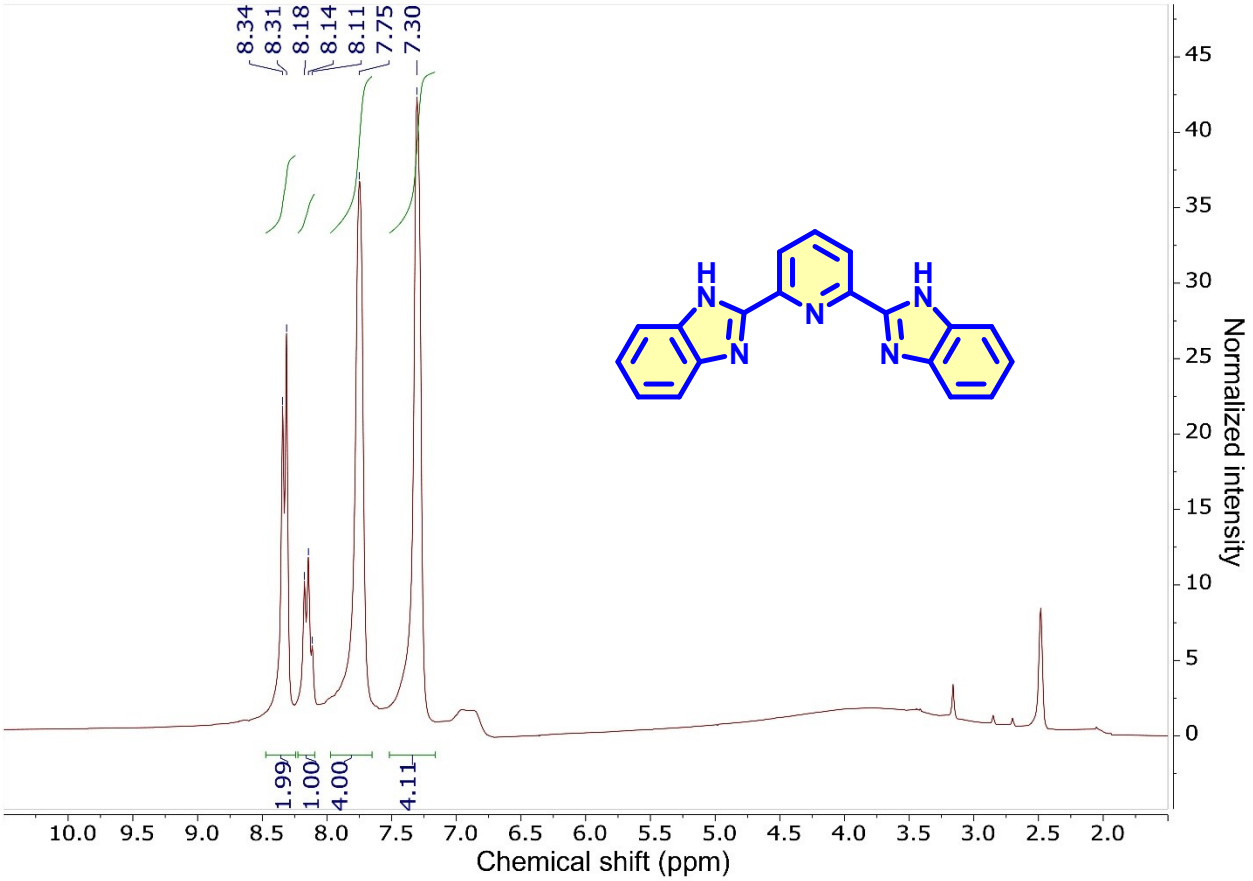

Figure S3: ^{1}H-NMR spectrum of 2,6-bis(1*H*-benzo[*d*]imidazol-2-yl)pyridine.

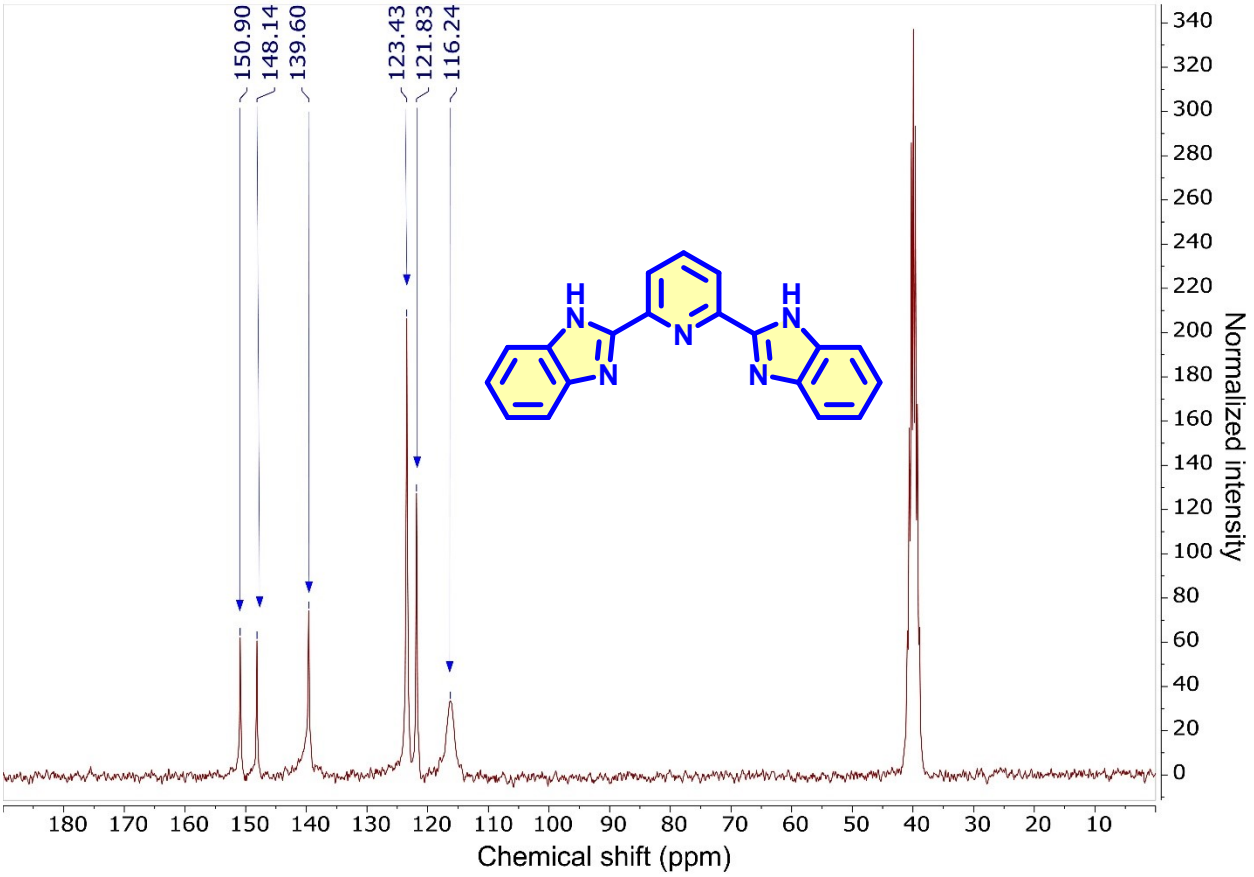

Figure S4: ^{13}C-NMR spectrum of 2,6-bis(1*H*-benzo[*d*]imidazol-2-yl)pyridine.

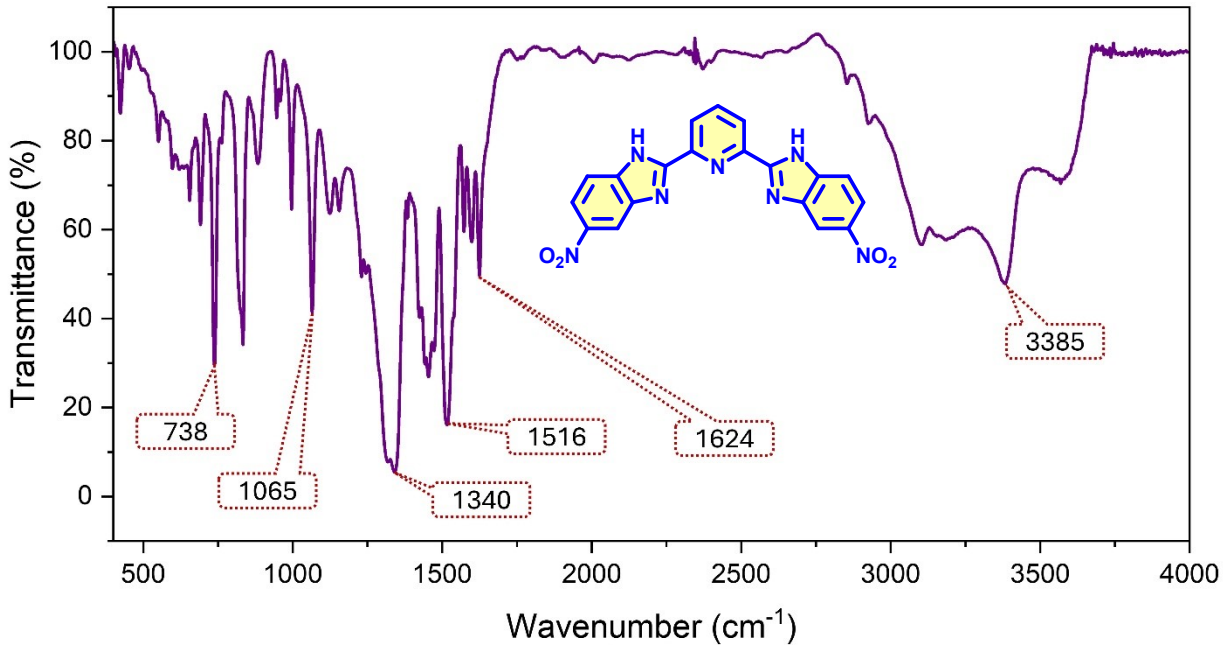

Figure S5: FT-IR spectrum of 2,6-bis(5-nitro-1*H*-benzo[*d*]imidazol-2-yl)pyridine.

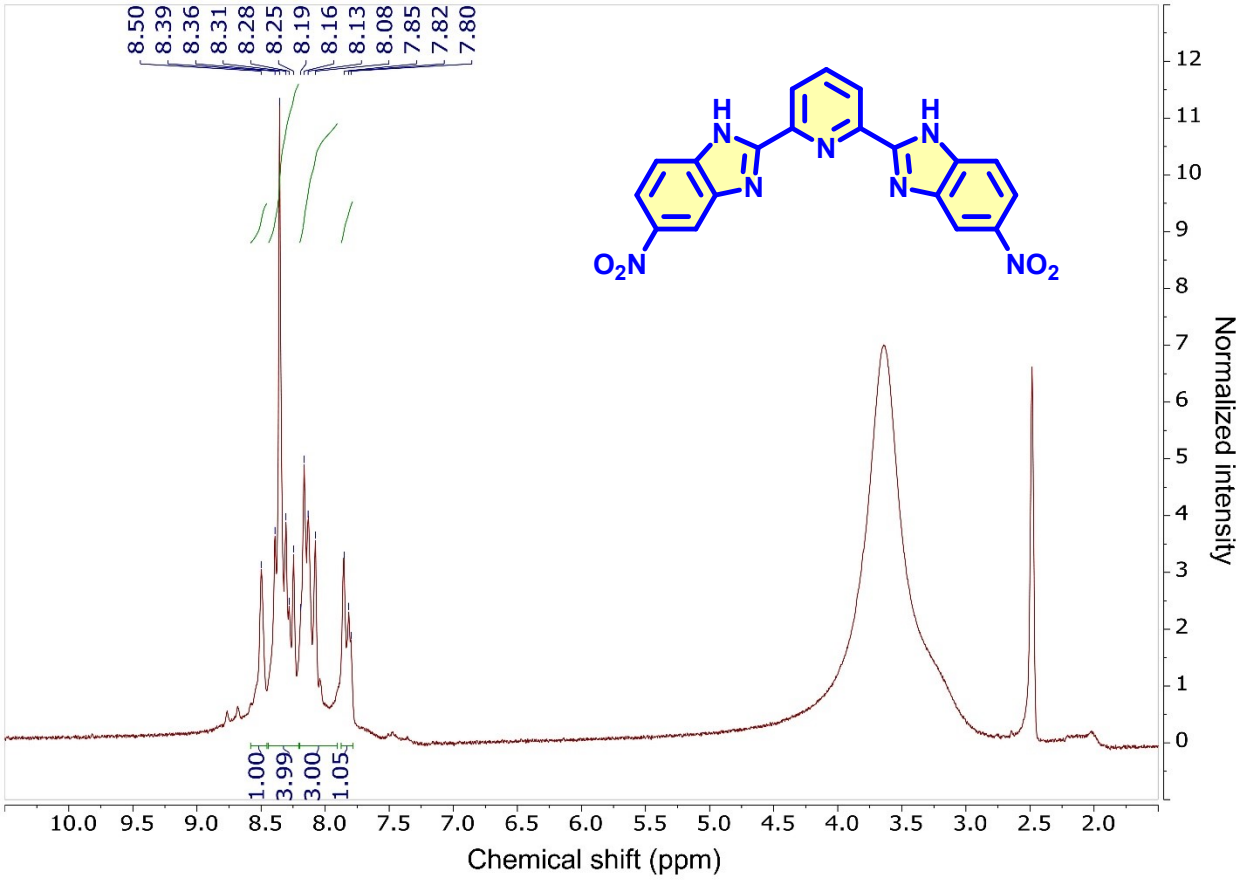

Figure S6: ^{1}H-NMR spectrum of 2,6-bis(5-nitro-1*H*-benzo[*d*]imidazol-2-yl)pyridine.

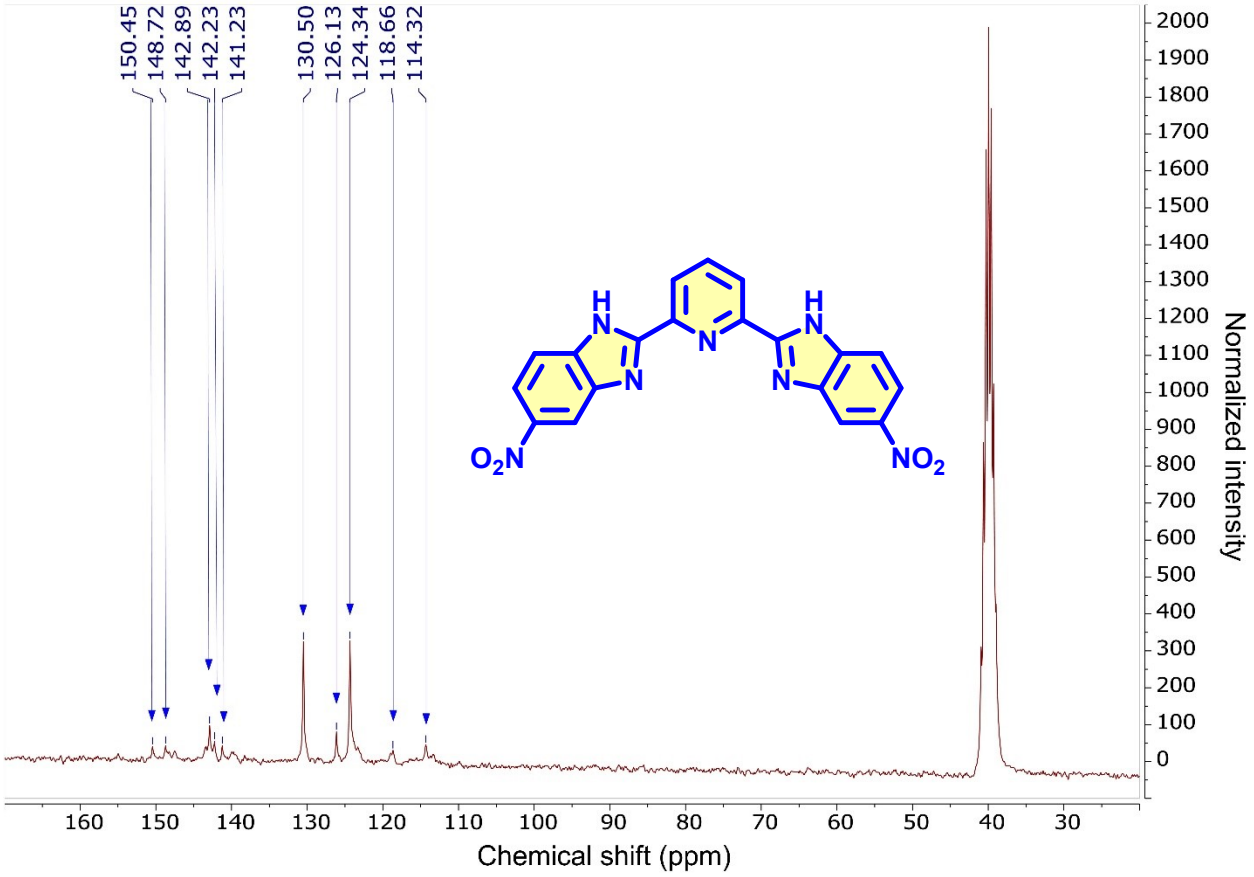

Figure S7: ^{13}C-NMR spectrum of 2,6-bis(5-nitro-1*H*-benzo[*d*]imidazol-2-yl)pyridine.

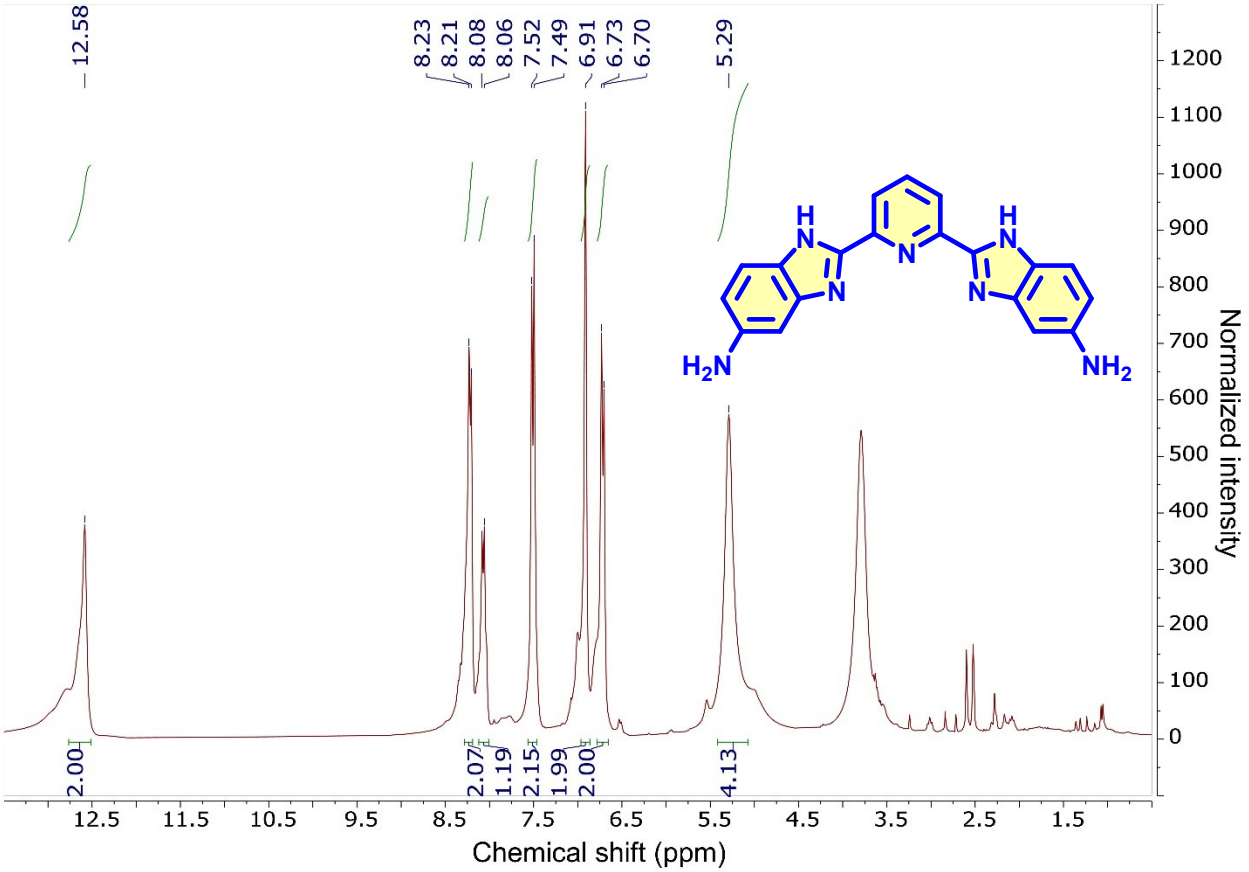

Figure S8: ^{1}H-NMR spectrum of Ligand-1.

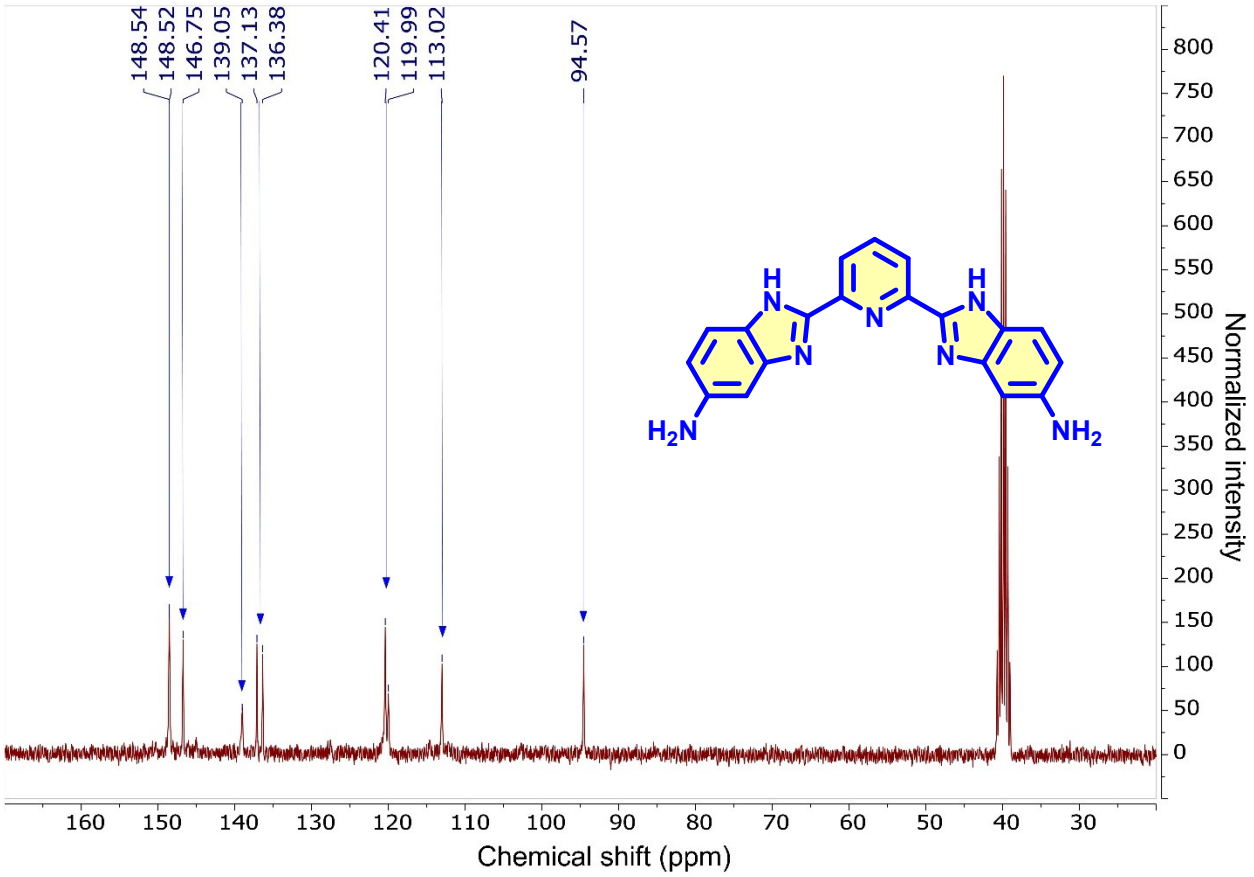

Figure S9: ^{13}C-NMR spectrum of Ligand-1.

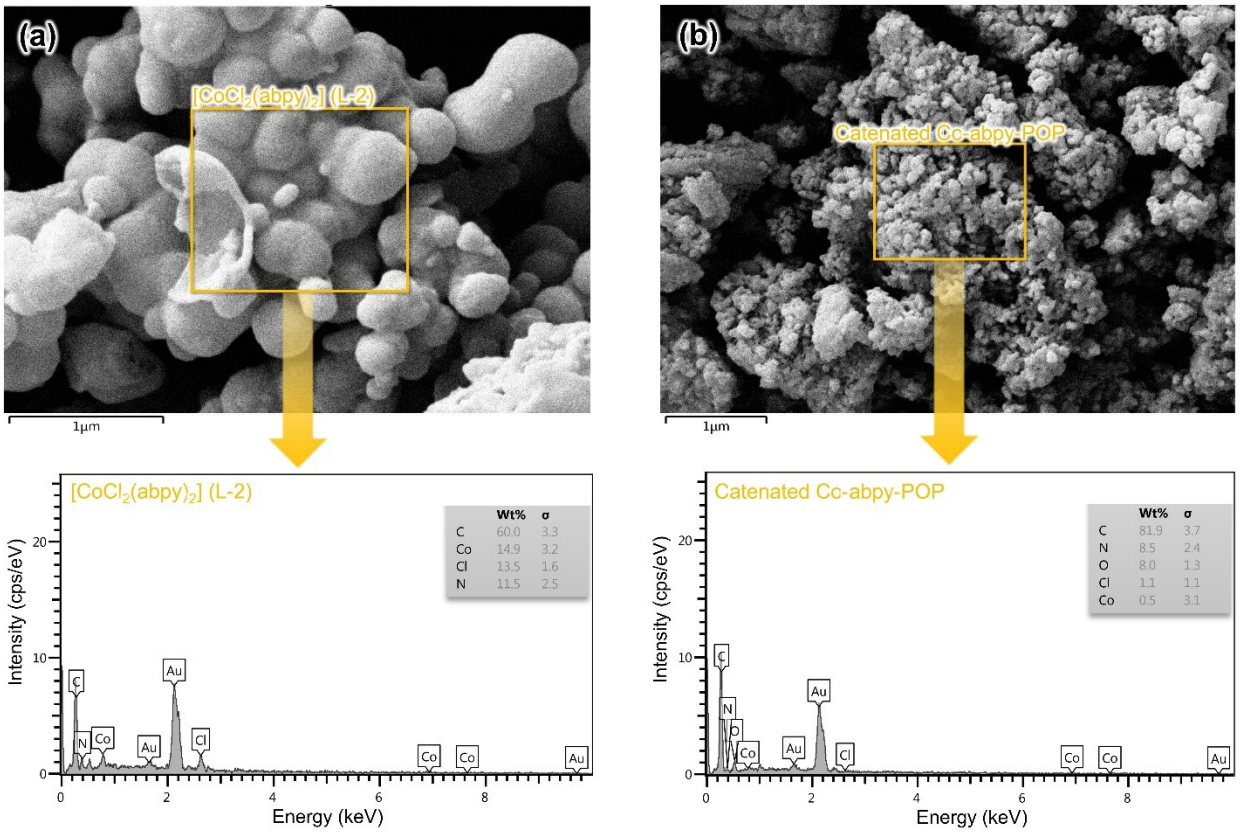

Figure S10: EDS signals of Ligand-2 (a) and Co-abpy-POP (b).

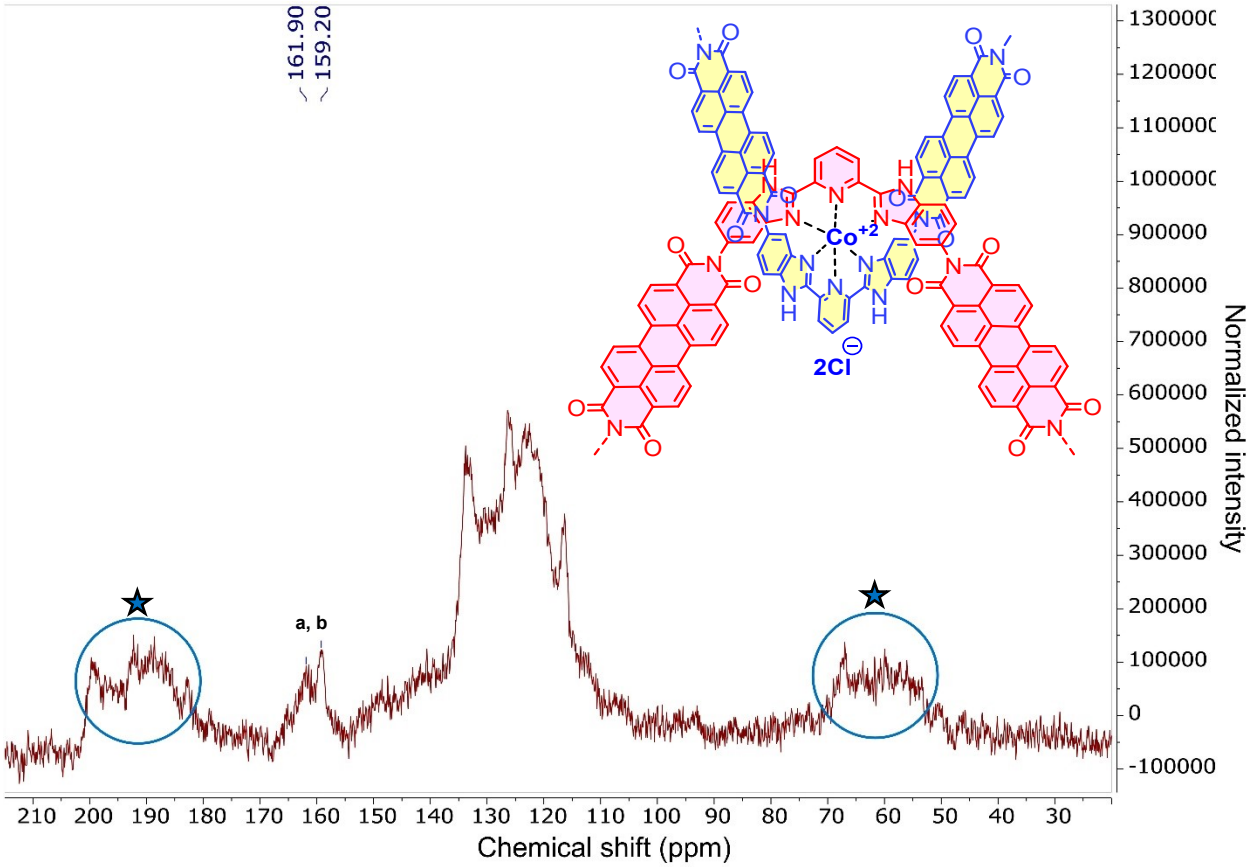

Figure S11: High-resolution solid-state ^{13}C-NMR spectrum of catenated Co-abpy-POP, asterisks denote spinning sidebands.

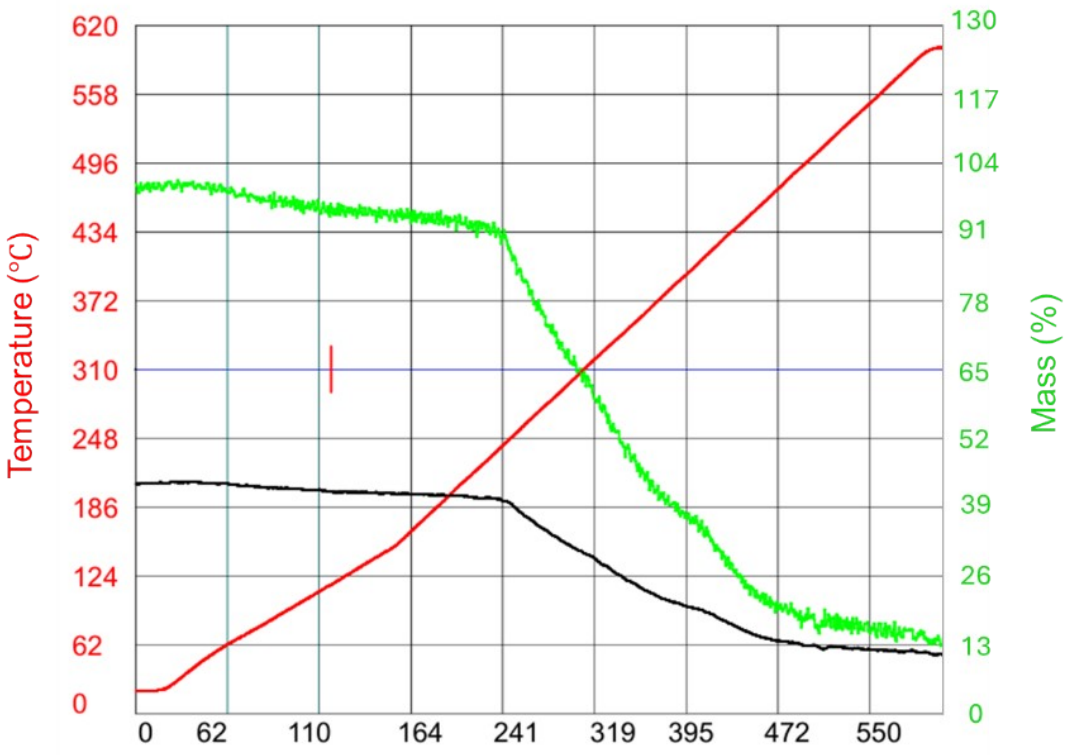

Figure S12: TGA analysis results of catenated Co-abpy-POP.

5. **Photothermal conversion and water desalination application by catenated Co-abpy-POP and Ligand-2 systems**

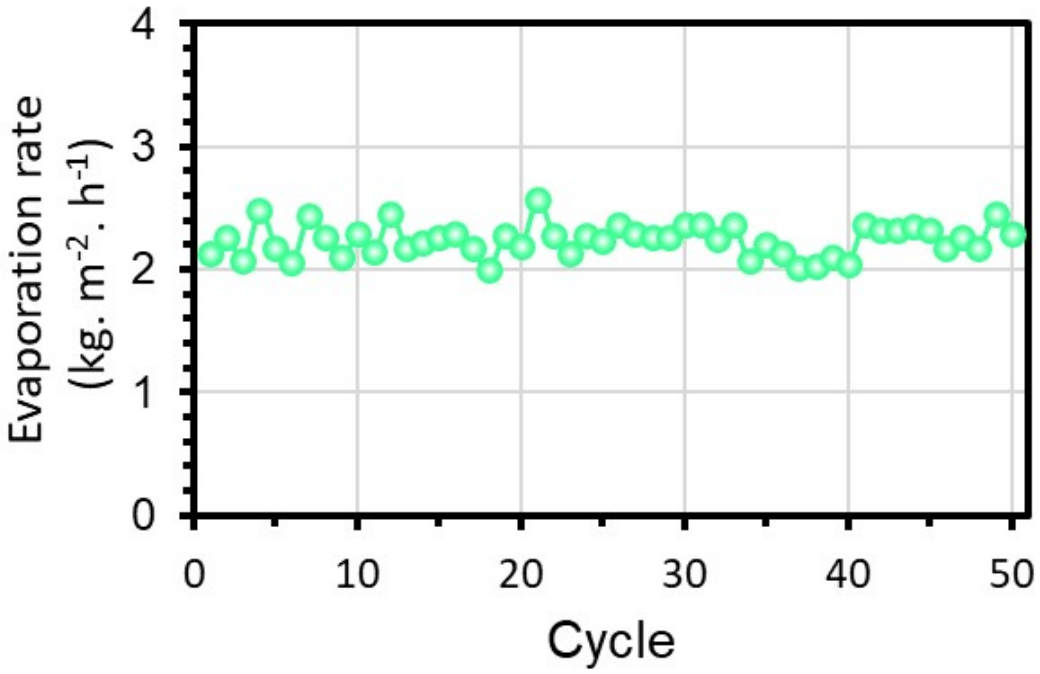

Figure S13: Performance stability of the Co-abpy-POP-based ISSG device under 1.0 sun illumination, for 50 cycles.

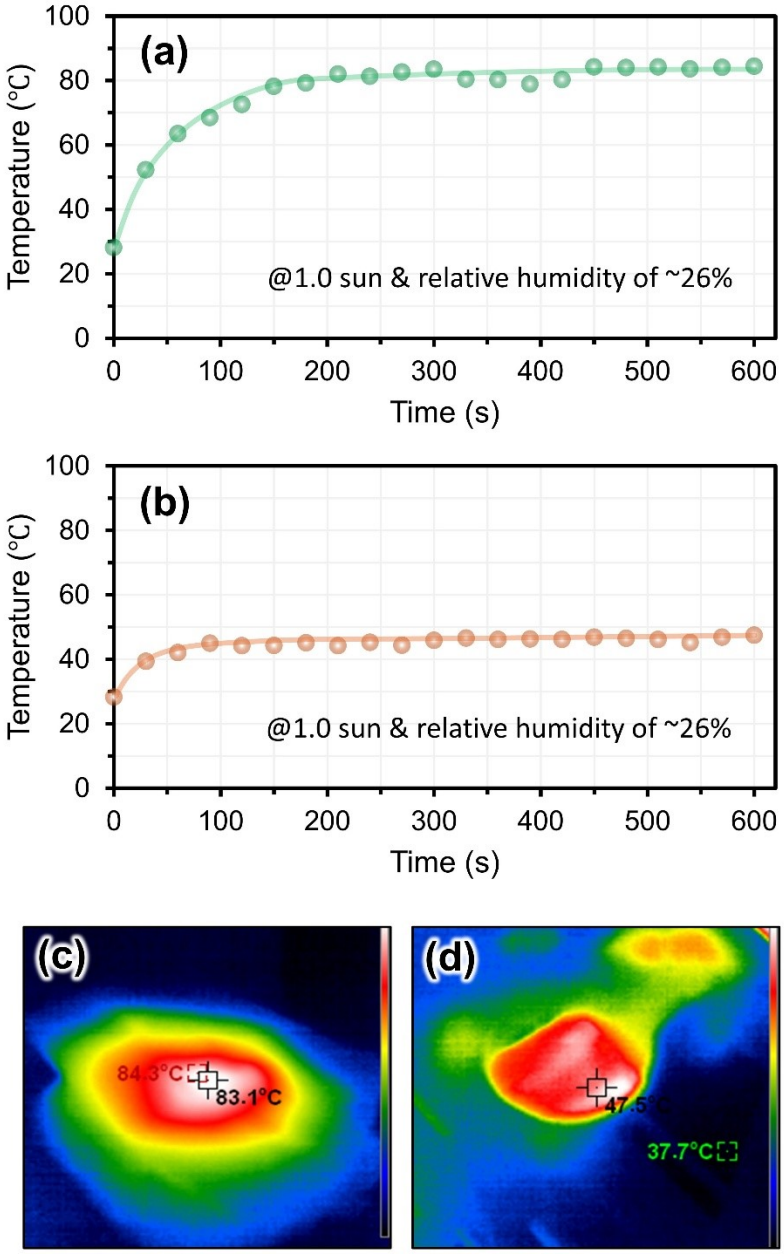

Figure S14: Surface temperature increasing results of dry catenated Co-abpy-POP (a) and Ligand-2 (b) under sunlight illumination during 600 s, the Infrared images of catenated Co-abpy-POP (c), and Ligand-2 (d) under the aforementioned conditions.

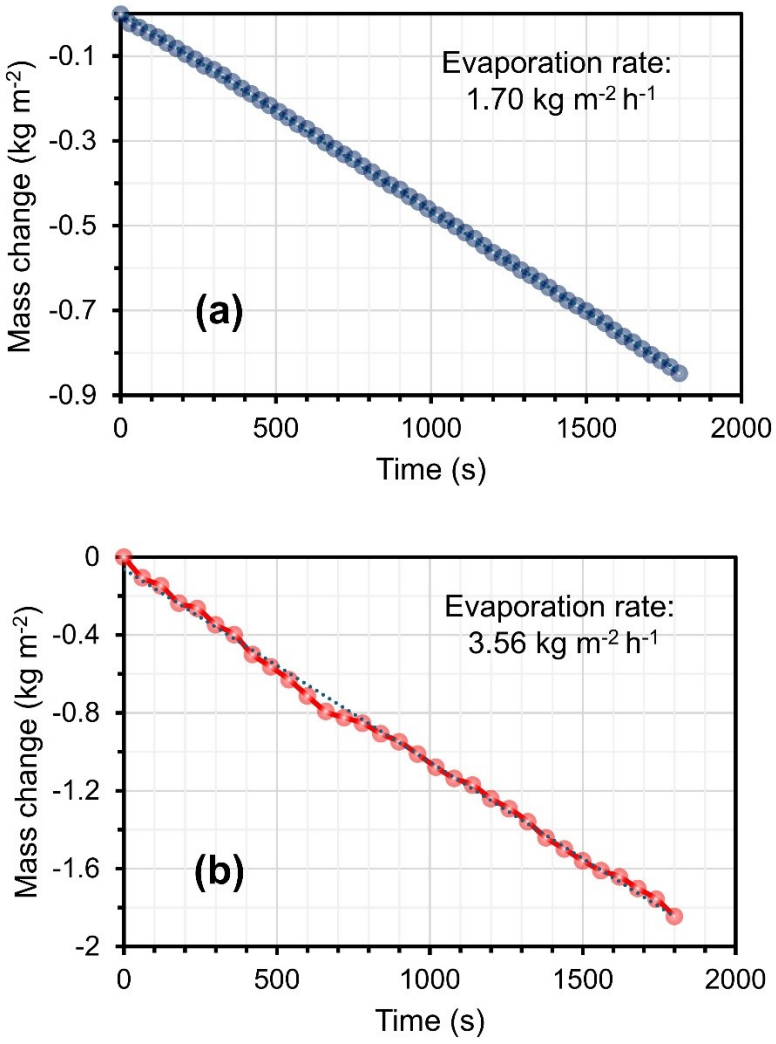

Figure S15: Mass change and evaporation rate of Ligand-2 (a) and catenated Co-abpy-POP (b) under sunlight irradiation.

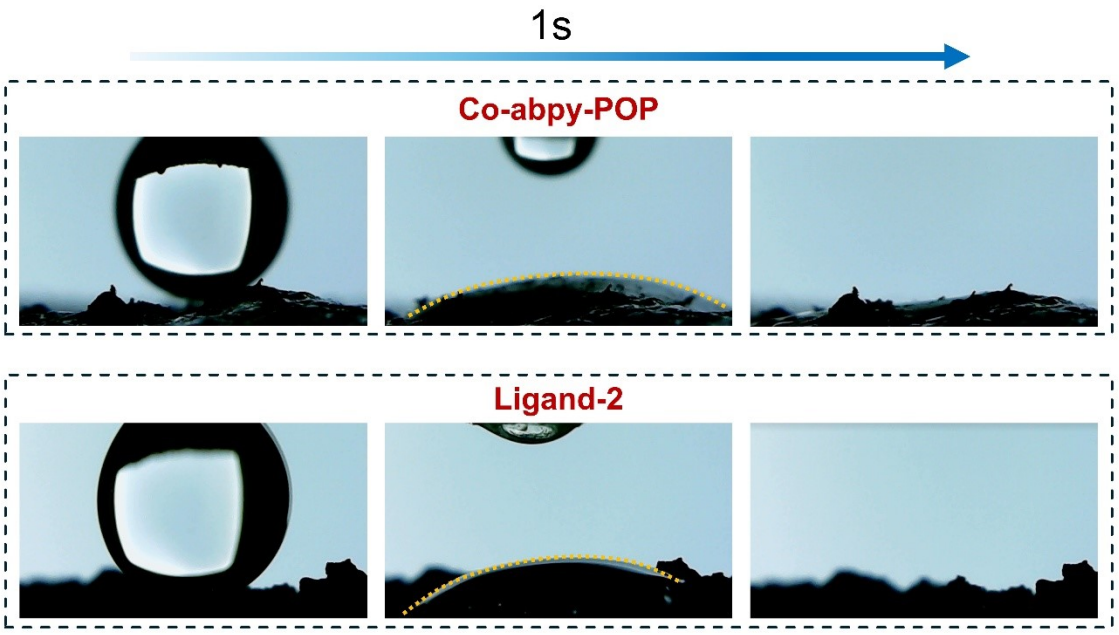

Figure S16: Photos of the wettability of catenated Co-abpy-POP and Ligand-2.

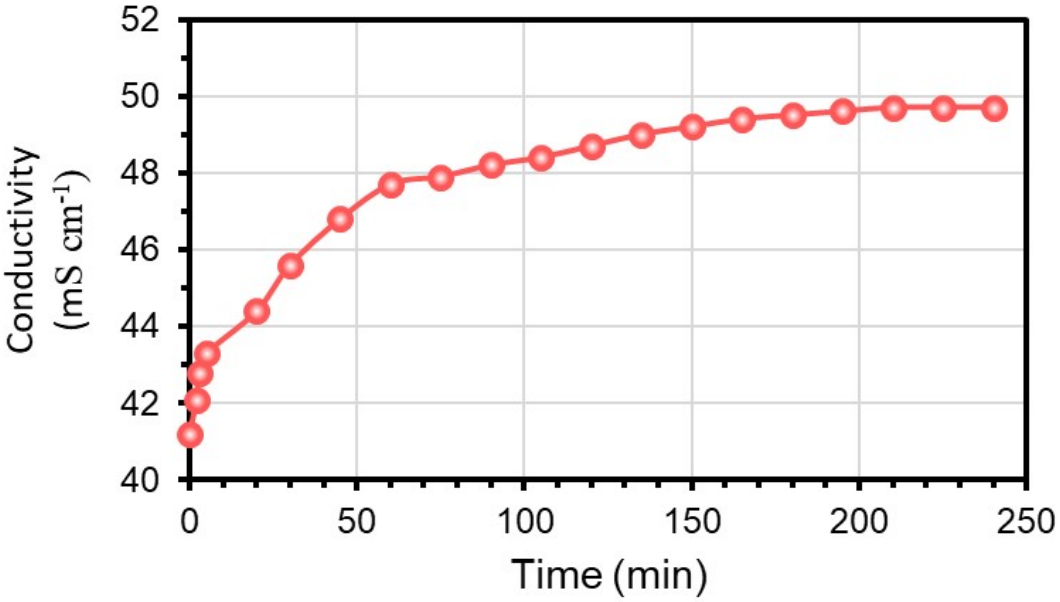

Figure S17: Conductivity increase of aqueous solution of ISSG setup over time under dark conditions due to dissolution of formed salt crystals on the sample surface.

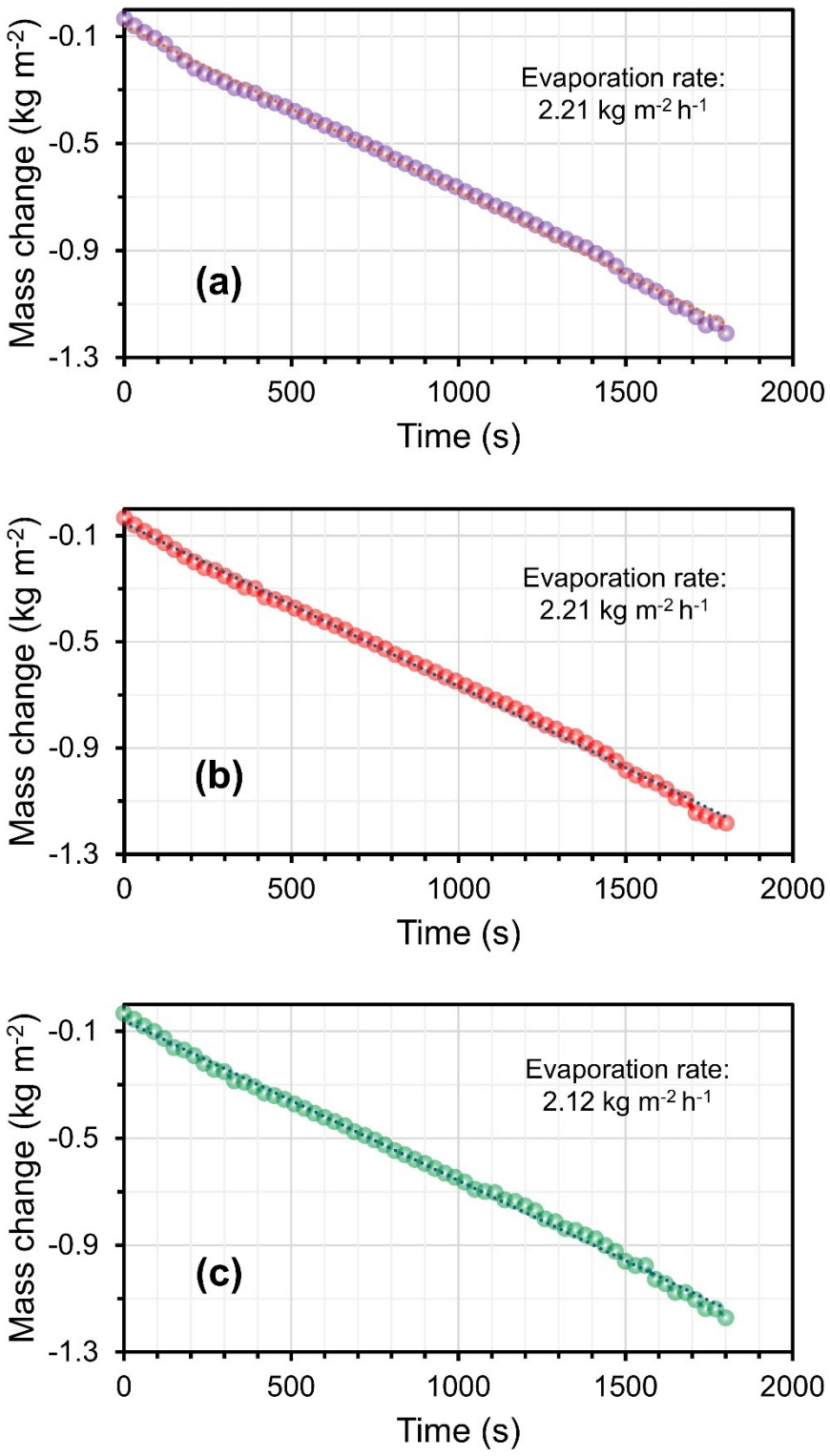

Figure S18: Water mass change and evaporation rate of catenated Co-abpy-POP for distilled water (a), 3% NaCl concentration (b), 10% NaCl concentration (c).

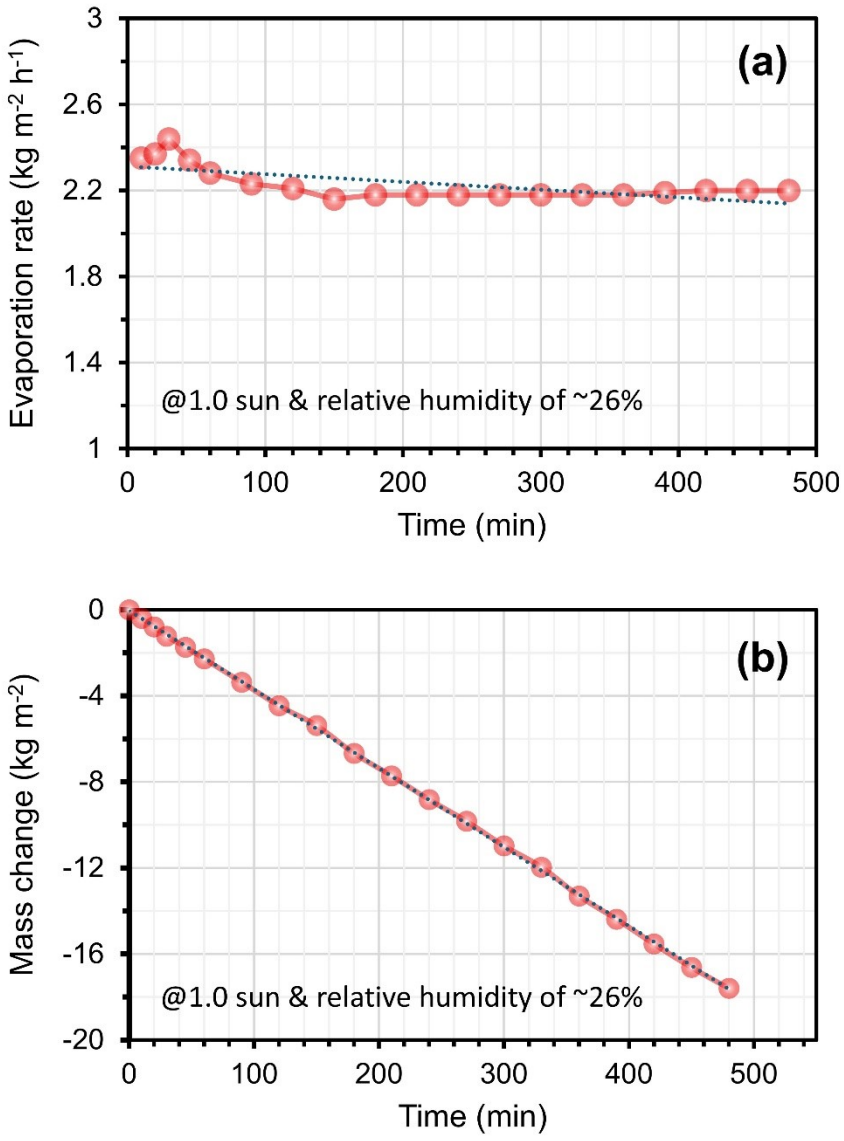

Figure S19: Investigating the stability of the evaporation rate of water using the catenated Co-abpy-POP system during 480 min (a), water mass change by the catenated Co-abpy-POP absorber under 1.0 sun irradiation during 8 h light irradiation (b).

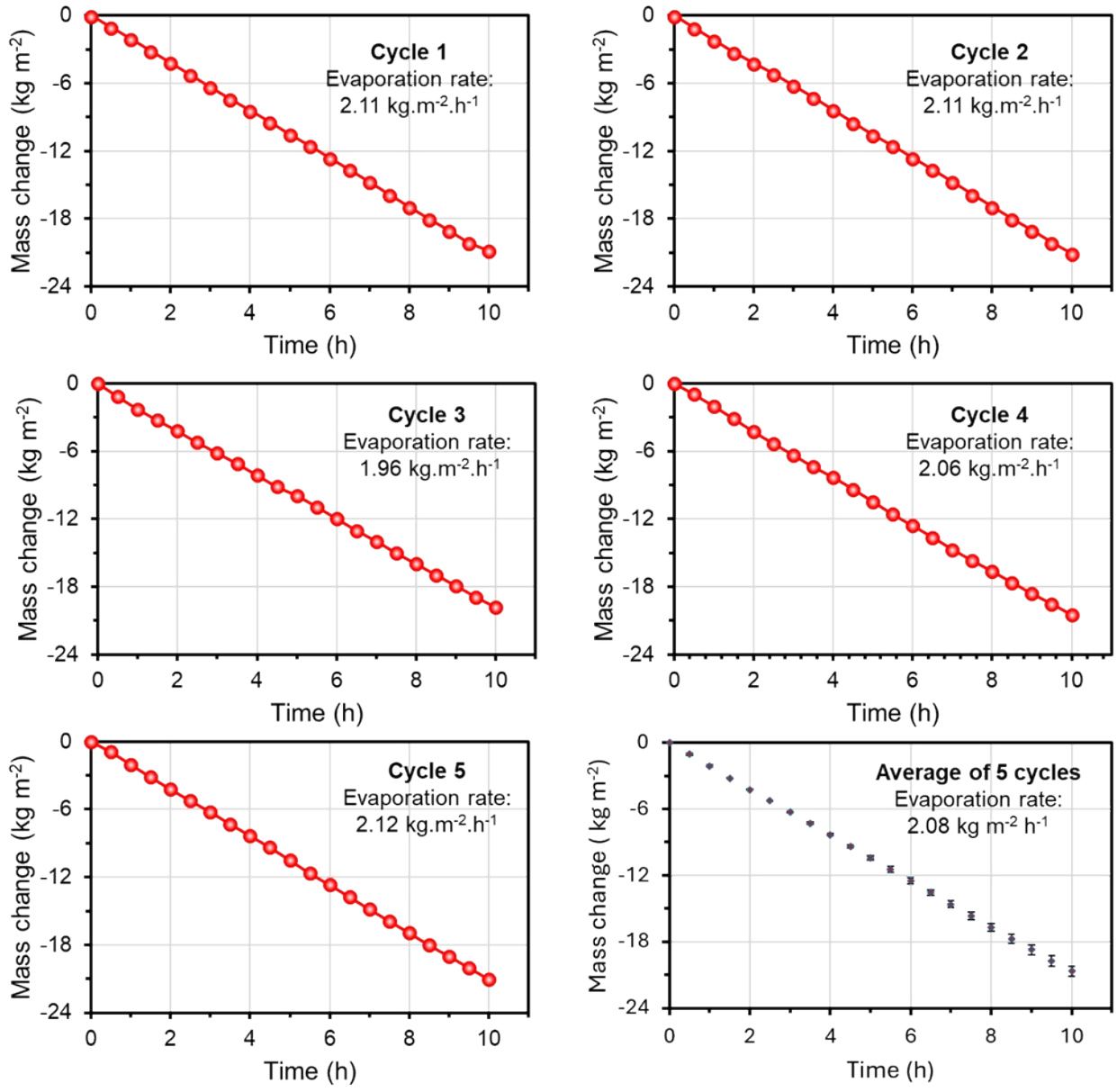

Figure S20: Mass change and evaporation rate of water using a 10% NaCl solution in the presence of catenated Co-abpy-POP for five cycles of 10 h continuous desalination and error bars are standard deviations for five cycles.

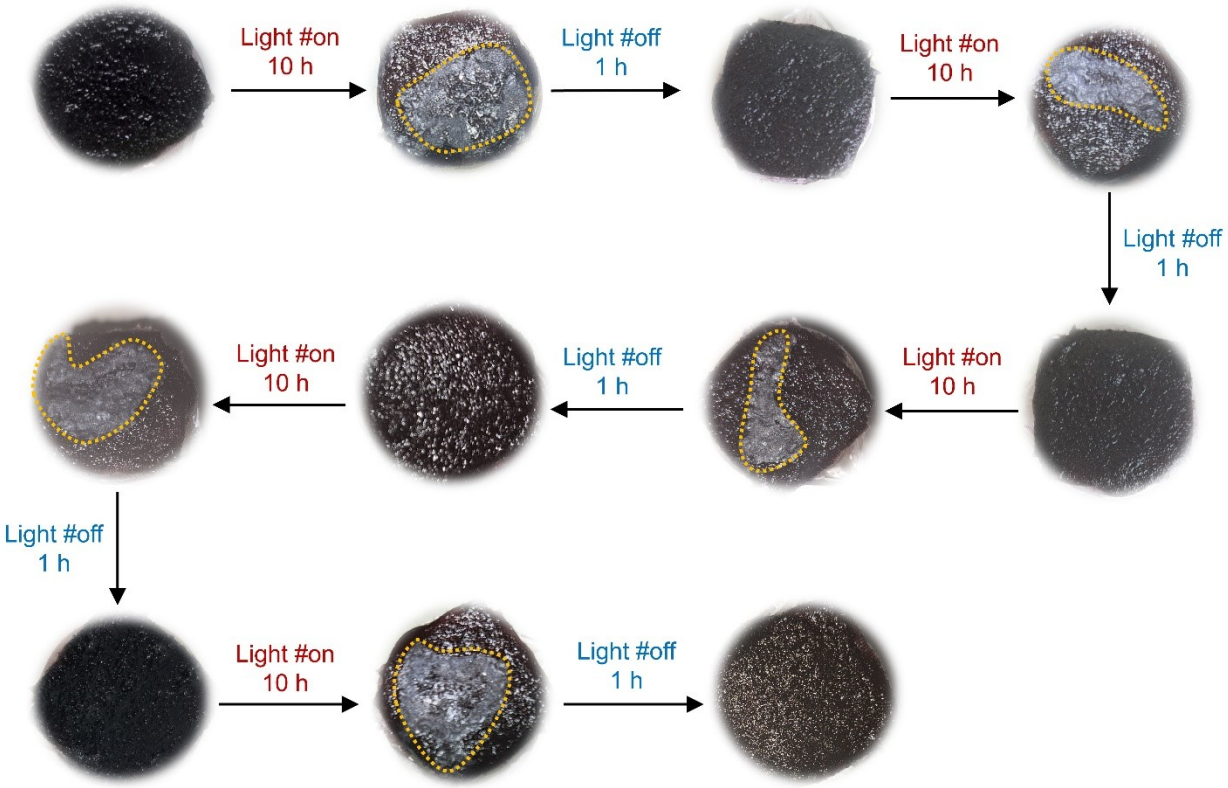

Figure S21: The images of the anti-salt fouling potential of catenated Co-abpy-POP for five cycles of 10 h continuous desalination and 1 h darkness condition.

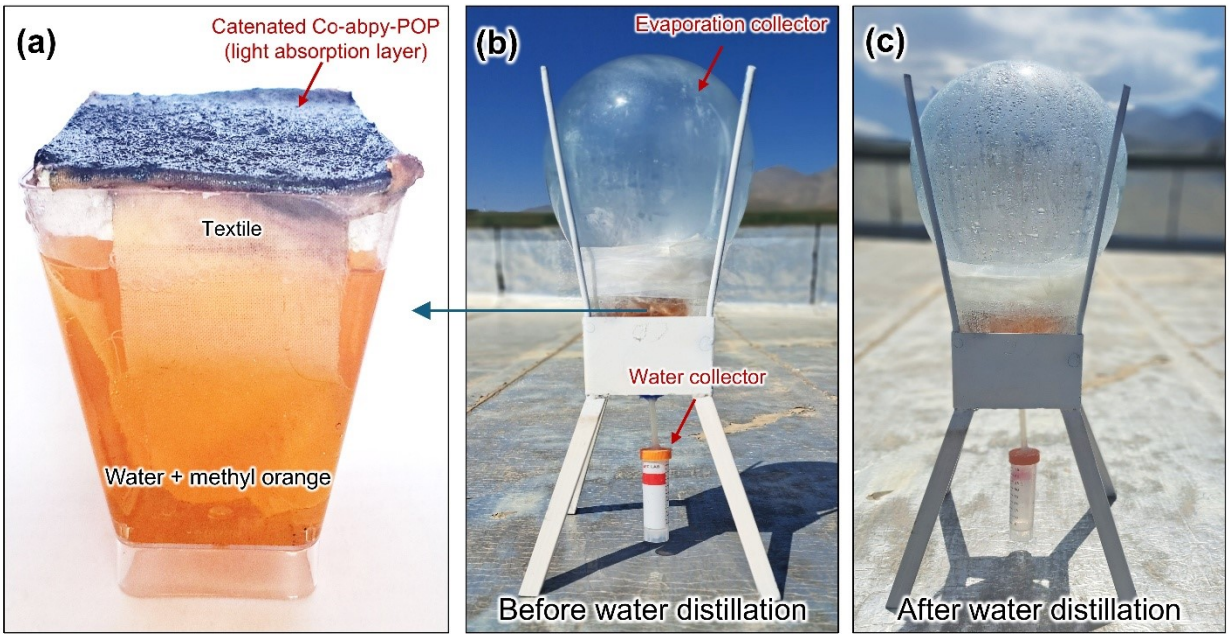

Figure S22: The image of the catenated Co-abpy-POP-based system used for photothermal water desalination and removal of methyl orange (a), the images of the condenser system containing catenated Co-abpy-POP-based solar steam generation and water collection, before (b) and after (c) sunlight irradiation.

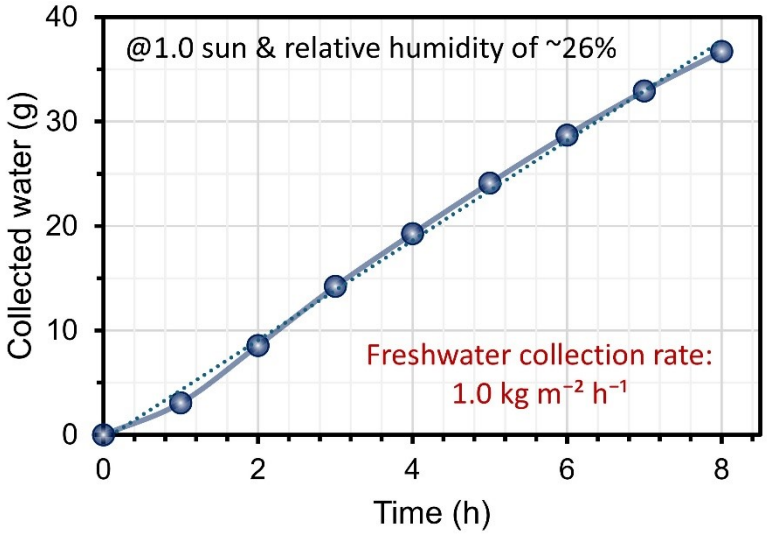

Figure S23: The diagram of collected water over time for catenated Co-abpy-POP-based solar water desalination.

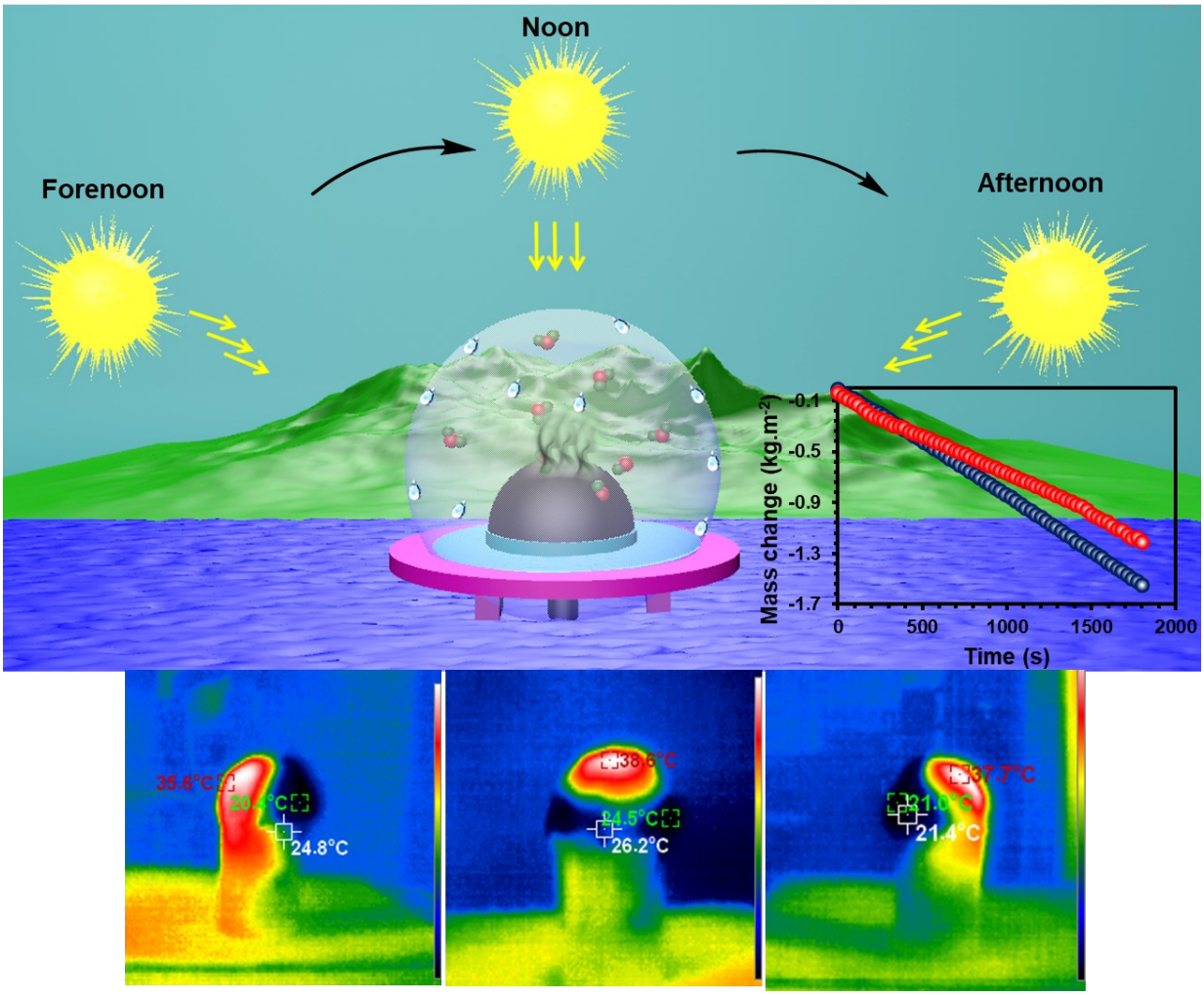

Figure S24: Schematic illustration of evaporator under varying sunlight angles (forenoon, noon, and afternoon), demonstrating stable photothermal performance of catenated Co-abpy-POP-based system throughout the day. Infrared thermal images showing surface heating under different illumination conditions. The plotted data compares water mass change over time for the catenated Co-abpy-POP-based system versus control setups, highlighting its enhanced evaporation capability.

6. Supplementary Note 3. Investigating the role of calcium alginate binder in adherence stability of Co-abpy-POP on the surface of cotton fabric.

Catenated Co-abpy-POP was coated on the surface of cotton fabric using calcium alginate hydrogel as a stable binder.[4] 1 mL of sodium alginate solution (3 wt%) and 2 mL of calcium chloride solution (0.1 M) were spread onto the surface of cotton fabric and dried at 60 ℃ for 30 min to create calcium alginate hydrogel on the surface of cotton fabric. Then, catenated Co-abpy-POP powder was coated onto the surface of cotton fabric containing calcium alginate binder, and it was subjected to ambient conditions for 30 min. In the next step, sodium alginate solution (3 wt%) and calcium chloride solution (0.1 M) were again spread on the surface of the system. The prepared system was applied for solar steam generation, and the obtained evaporation rate is 2.08 $kg.m^{-2}$ h^{-1} (Figure S25). Also, due to washing the catenated Co-abpy-POP –calcium alginate system by a water stream, no release of catenated Co-abpy-POP particles was observed, indicating the desirable physical stability of this system (Figure S26).

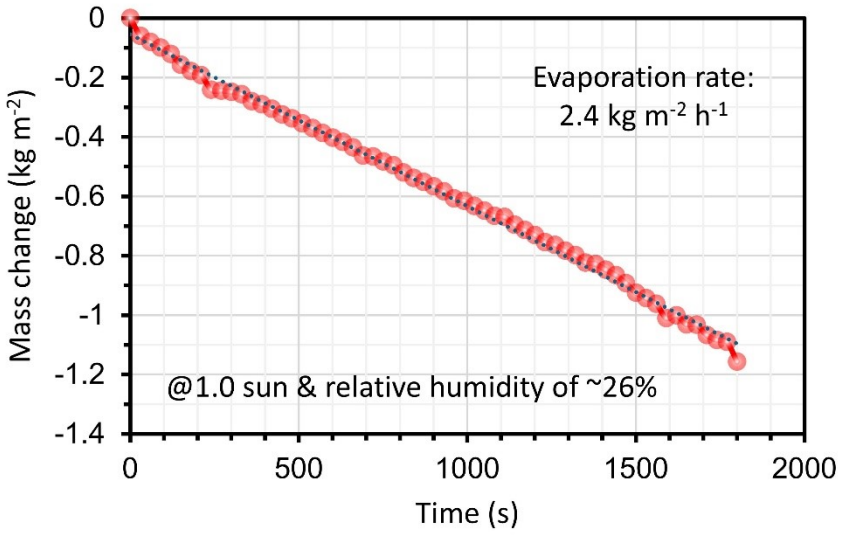

Figure S25: Mass change and evaporation rate of catenated Co-abpy-POP decorated on cotton fabric by using calcium alginate hydrogel as binder.

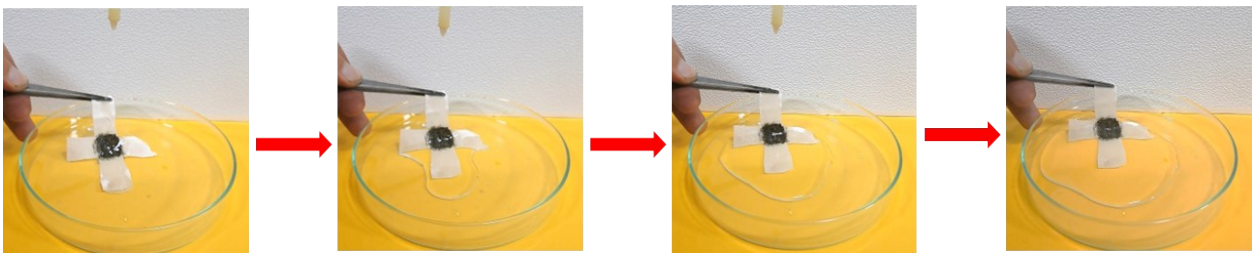

Figure S26: The confirmation of adherence stability of catenated Co-abpy-POP coated on cotton fabric using calcium alginate binder during washing by the water stream.

7. Characterization and investigating the role of abpy-POP in ISSG process

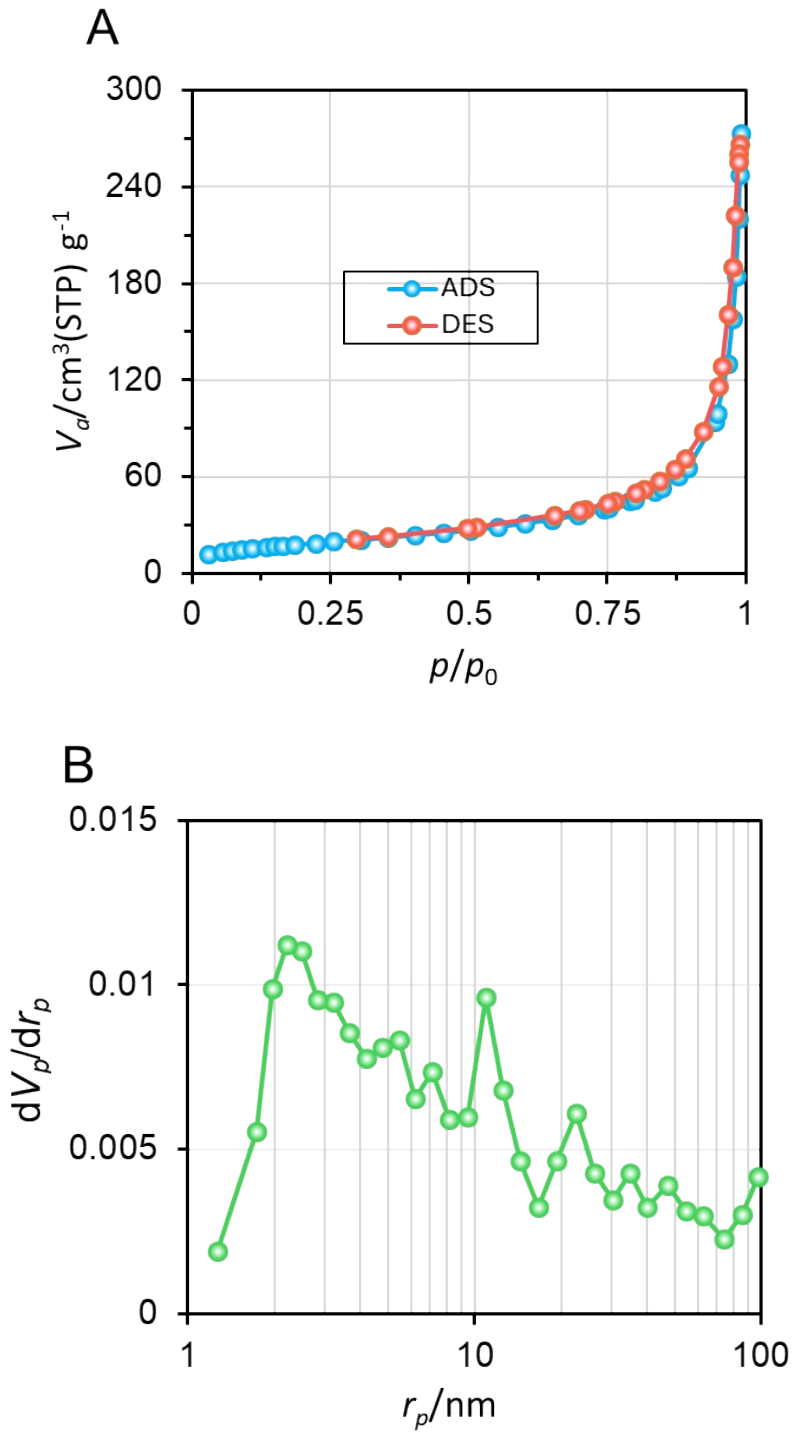

Figure S27: (A) N_2 adsorption–desorption isotherms and (B) pore size distribution of abpy-POP

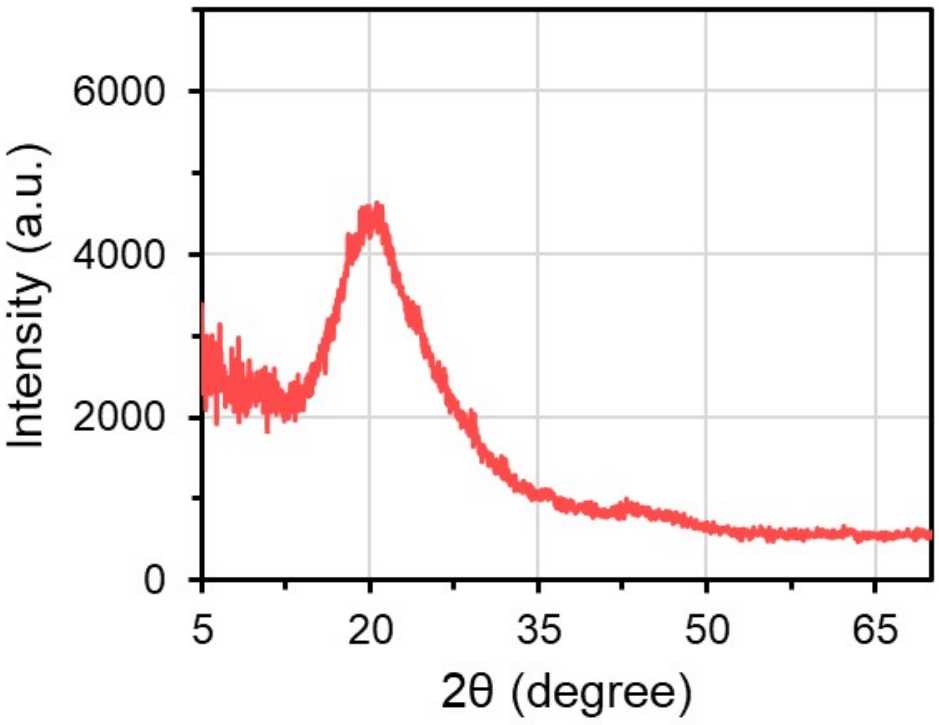

Figure S28: XRD pattern of abpy-POP, indicating its amorphous structure

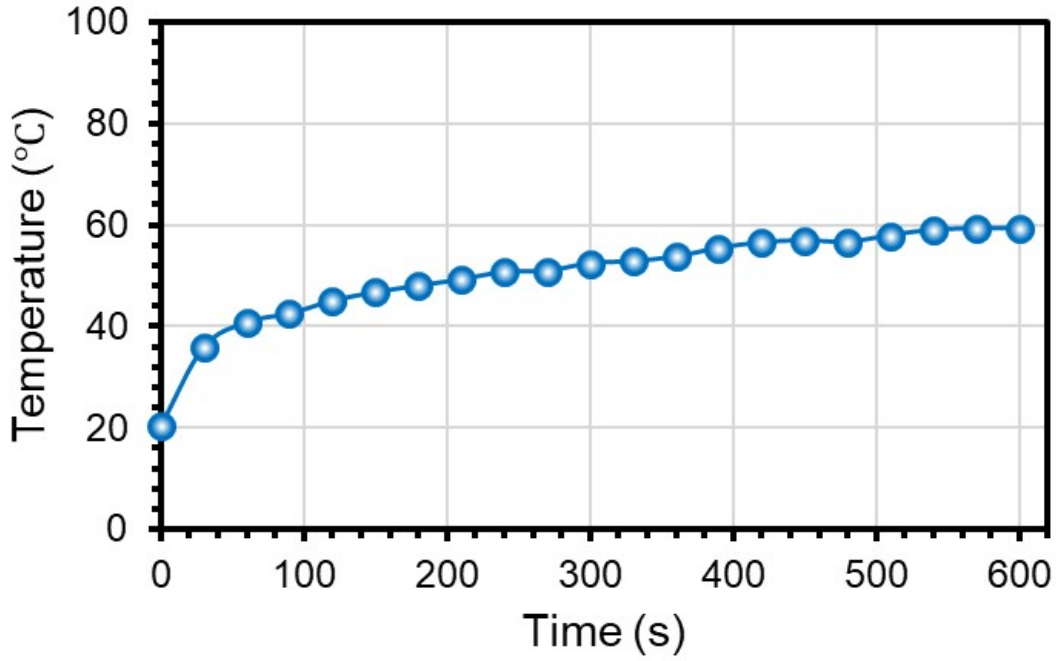

Figure S29: Surface temperature increasing curve of dry abpy-POP under 1.0 sun illumination during 600 s

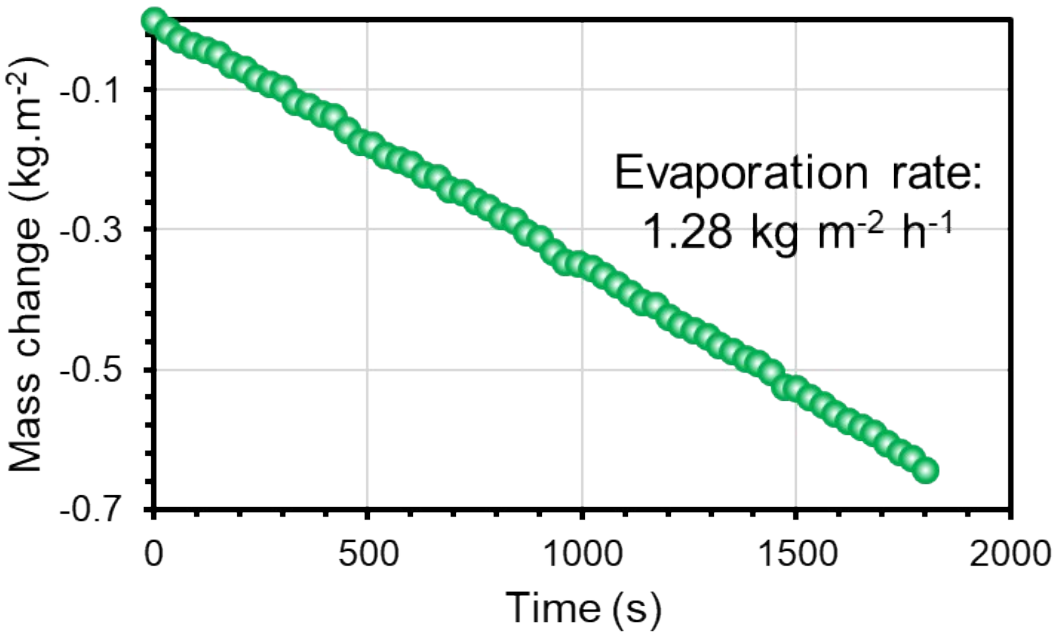

Figure S30: Mass change and evaporation rate of abpy-POP under 1.0 sun irradiation

8. Comparing the performance of Co-abpy-POP and reported systems (1.0 sun)

Table S1: Comparison of the performance of Co-abpy-POP upon the solar steam generation by the previously reported systems under 1.0 sun irradiation.

Entry	*Solar absorber*	*Evaporation rate (kg m^{-2} h^{-1})*	*Reference*
1	**Co-abpy-POP**	**2.22**	**This work**
2	PySQ-COF	1.35	[5]
3	COF-Azu-TP	1.43	[6]
4	TPAD-COF	1.42	[7]
5	thiazole-linked COF	0.744	[8]
6	MoCOF@Gel	2.31	[9]
7	benzoxazole-linked COF	1.39	[10]
8	Porous ionic polymers coated with polypyrrole	1.41	[11]
9	PMDA-TAPA COF	1.47	[12]
10	rGO-COF	1.47	[13]
11	Polymer E-DTP	2.1	[14]

9. Investigation of the stability of Co-abpy-POP by using XPS analysis

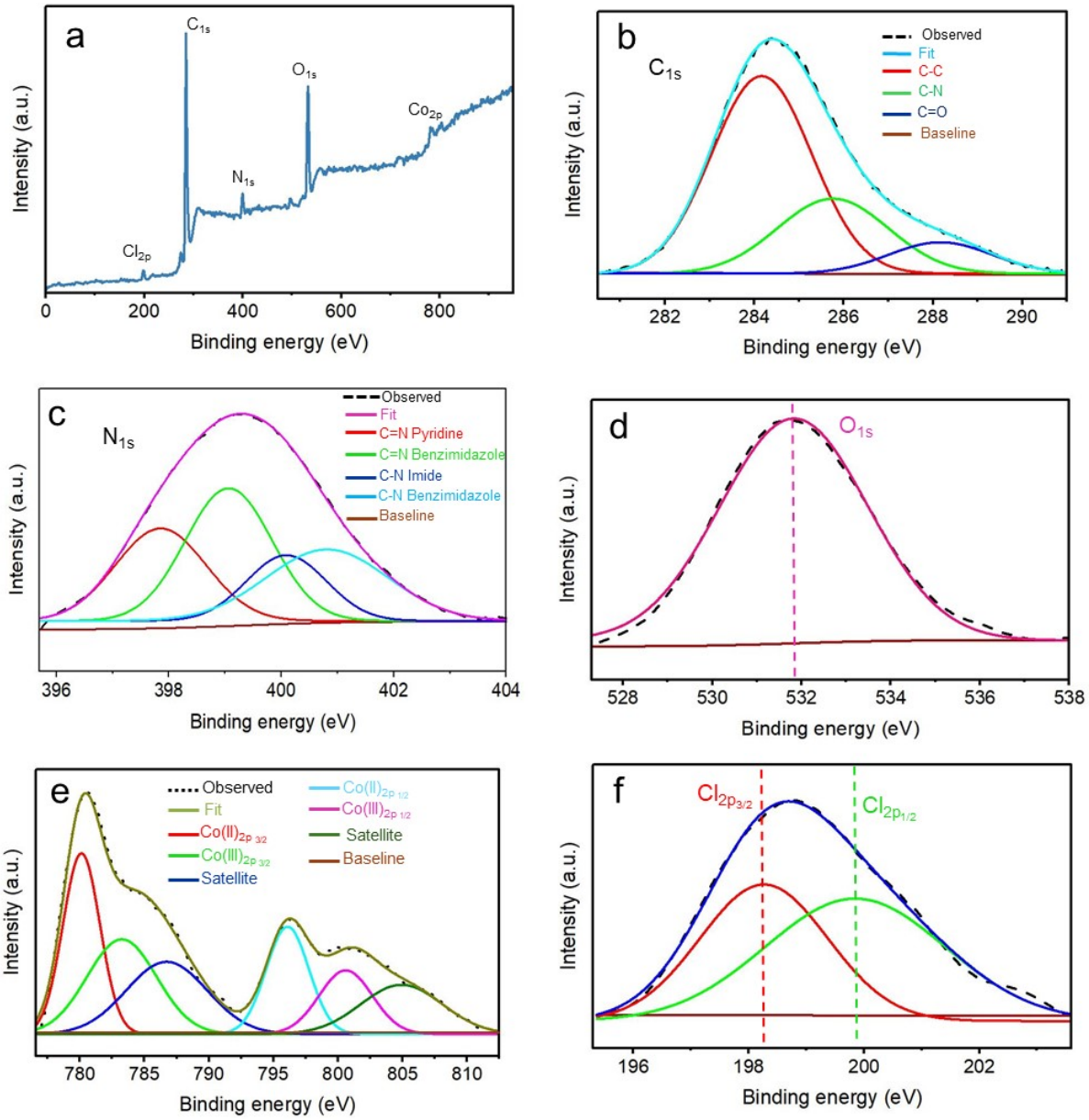

Figure S31: (a) XPS survey spectrum of Co-abpy-POP showing peaks for C, N, O, Co, and Cl. (b) High-resolution C(1s) XPS spectrum peaks. (c) High-resolution N(1s) XPS spectrum peaks. (d) High-resolution O(1s) XPS spectrum peak. (e) High-resolution Co(2p) XPS spectrum displaying Co(II)($2p_{3/2}$), Co(III)($2p_{3/2}$), Co(II)($2p_{1/2}$), and Co(III)($2p_{1/2}$) peaks. (e) High-resolution Cl(2p) XPS spectrum showing Cl($2p_{3/2}$) and Cl($2p_{1/2}$) peaks.

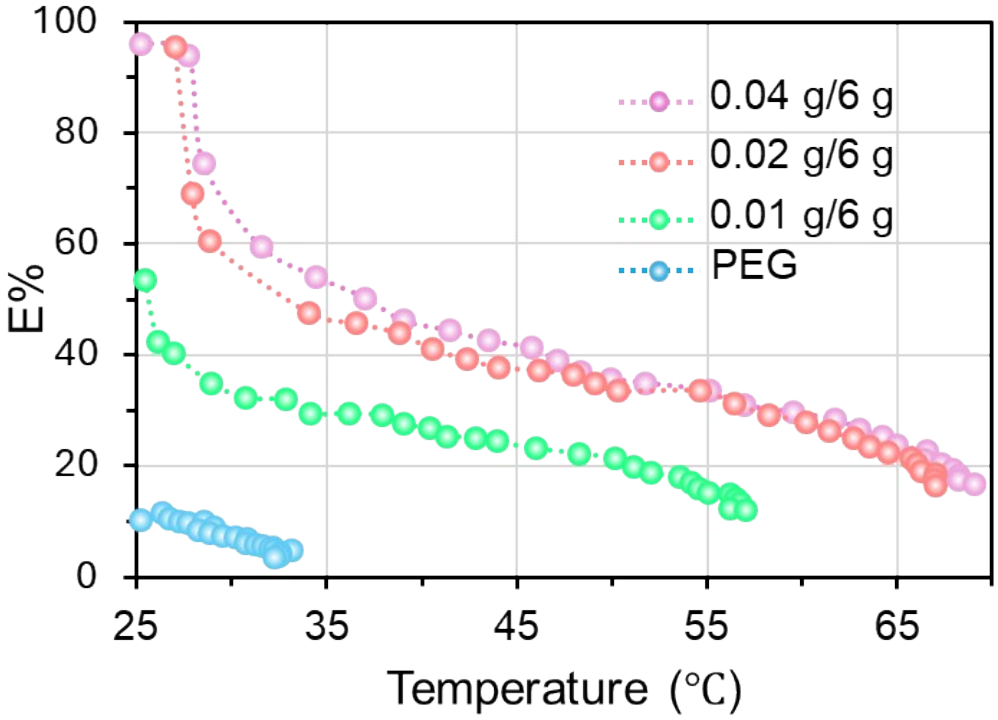

Figure S32: The *E%* of the Co-abpy-POP-based nanofluids with different concentrations (0.01, 0.02, and 0.04 g per 6 g PEG) and pure PEG solution versus temperature.

Table S2: *Comparison of performance of Co-abpy-POP and some of reported materials in DASC*				
Entry	**Solar collector**	**E%(max)**	**E%(min)**	**Reference**
1	**Co-abpy-POP**	**96**	**17**	**This work**
2	CuO/Ag	96.11	39.58	[15]
3	V/PEG	~100	20	[16]
4	Cr	82	~20	[17]
5	Mo	54	~20	[17]
6	W	53	18	[17]
7	Lignin/PEG	80	18	[18]
8	Phosphonium ionic liquid	93	15	[19]
9	Magnetic Phosphonium ionic liquid	98	32	[19]
10	Pt	82	17	[20]
11	carbon quantum dot	~99	14	[21]
12	TiN@rGO	62	-	[22]

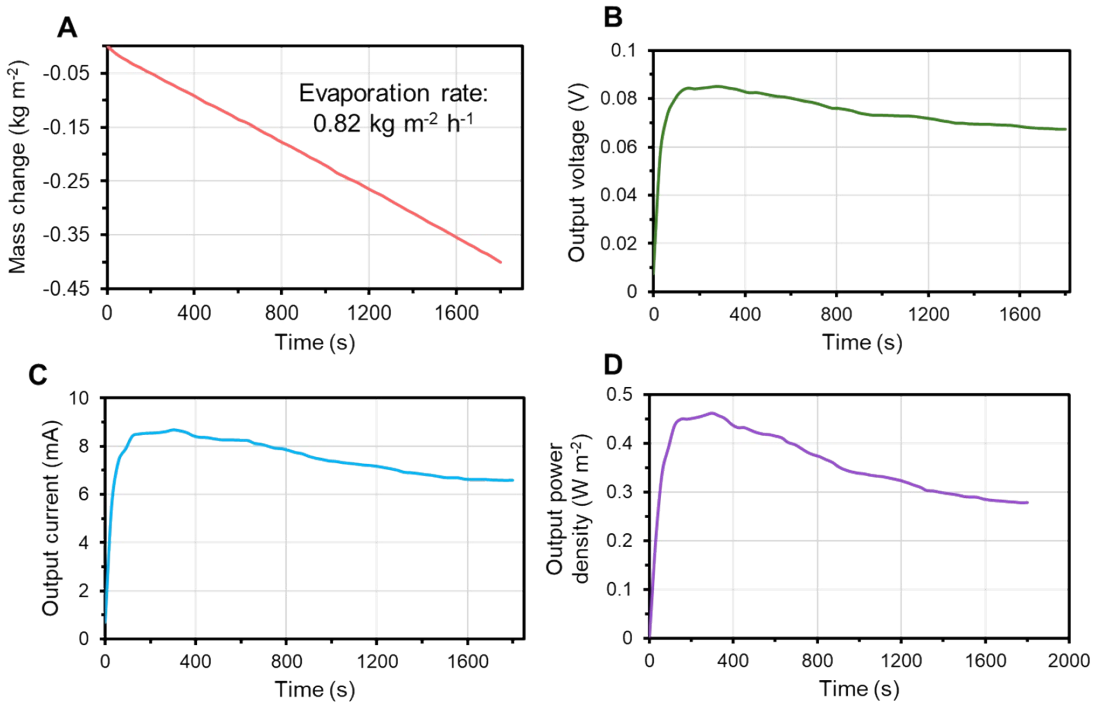

Figure 33: (A) Mass change and evaporation rate of water in Co-abpy-POP-based hybrid ISSG+PTE, (B) the output voltage, (C) output current and (D) output power density of Co-abpy-POP-based hybrid ISSG+PTE

Table S3: *Comparison of the output power density of Co-abpy-POP with some of reported PTE systems under 1 sun illumination*			
Entry	**PTE device**	**Power density ($W.\ m^{-2}$)**	**Reference**
1	**Co-abpy-POP**	**2.51**	**This work**
2	$\{[Ni_4Cl_2(ONDI)_2(bpy)_4]\cdot 2Cl\cdot 2H_2O\cdot xDMF\cdot yH_2O\}_n$	0.53	[23]
3	semiconductive hydroxamate coordination polymer	1.66	[24]
4	TQC@TEC1−12701	2.21	[25]
5	ReS_2@carbon framework	1.34	[26]
6	Ultra black carbon	0.6	[27]
7	Bi_2S_3/Pd	0.7	[28]
8	Au@Bi_2MoO_6-CDs	0.97	[29]
9	PT/RC-TE	1.55	[30]
10	tannic acid–Fe^{3+}–graphene oxide	1.92	[31]
11	Cu_2-xS nanosheets on copper foil	1.13	[32]

10. Supplementary Note 4. Calculation section

Based on our recent work,[33] and considering mass change of Ligand-2 and catenated Co-abpy-POP (m_{dark}), mass change of bulk water ($m_{0,dark}$), both in dark condition and the same geometric area (A_{proj}=3.14 cm^2), the evaporation area (A_{evap}) was calculated based on the following equation:

$$A_{evap} = \frac{m_{dark}}{m_{0,dark}} A_{proj} \quad (1)$$

By using equation 1 and Table S4 information, the calculated A_{evap} for Ligand-2, catenated Co-abpy-POP and cotton fabric are 6.93, 7.47, and 5.69 cm^2, respectively.

Table S4: The mass change results of bulk water, cotton fiber, Ligand-2, and catenated Co-abpy-POP under dark conditions and 1.0 sun irradiation within 30 min.

	Bulk water	***Cotton fiber***	***Ligand-2***	***Catenated Co-abpy-POP***
$m_{darkness}$ (g)	0.0430	0.078	0.095	0.1023
m_{1sun} (g)	0.0837	0.138	0.1853	0.3854

The modified evaporation rate ($\dot{m}'$) was calculated based on equation 2. m is mass change, and t is evaporation time.

$$\dot{m}' = \frac{m}{t\, A_{evap}} \quad (2)$$

Therefore, the calculated $\dot{m}'$ values for all four systems at 1 sun irradiation are as follows:

$\dot{m}'$ for Ligand-2 = 0.53 kg.h^{-1}.m^2

$\dot{m}'$ for catenated Co-abpy-POP= 1.03 kg.h^{-1}.m^2

$\dot{m}'$ for cotton fabric = 0.48 kg.h^{-1}.m^2

Heat loss calculation

The calculated radiation heat loss (P_{rad}) for catenated Co-abpy-POP is based on the Stefan-Boltzmann law:

$$P_{rad} = \varepsilon\sigma(T_2^4 - T_1^4) \quad (3)$$

ε is the emissive and is 0.847, σ is the Stefan-Boltzmann constant (5.67×10^{-8} W m^{-2} K^{-4}), T_2 is the temperature of the surface (34 °C), T_1 is the temperature of the environment (21 °C), and the light intensity is 1000 W m^{-2}. Therefore, the radiation heat loss is 9.4%.

The conduction heat loss (P_{con}) was calculated by using equation 4.

$$P_{con} = Cm^{\Delta T/At} \quad (4)$$

m is the weight of bulk water (0.005 kg), C is the specific heat capacity of pure water (4.2 J kg^{-1} °C^{-1}), ΔT is the difference between the temperature of bulk water at first and after the illumination time (t) (3 °C in 1800 s), and A is the projected area (0.000314 m^2). Therefore, the conduction heat loss is 0.01%.

The convection heat loss was calculated by using Newton's law:

$$P_{conv} = h(T_2\text{-}T_1) \quad (5)$$

The h is the convection heat transfer coefficient (≈5 W m^{-2} K^{-1}), T_2 is the temperature of the surface (34 °C), and T_1 is the temperature of the environment (21 °C). Accordingly, the convection heat loss is 6.5%.

11. References

1. Zolfigol, M.A., Azizian, S., Torabi, M., Yarie, M., and Notash, B. (2024). The importance of nonstoichiometric ratio of reactants in organic synthesis. J. Chem. Educ. *101*, 877–881.

2. Wang, L., Polyansky, D.E., and Concepcion, J.J. (2020). Self-assembled bilayers as an anchoring strategy: Catalysts, chromophores, and chromophore-catalyst assemblies. J. Am. Chem. Soc. *141*, 8020–8027.

3. Shivaji Padmor, M., Vishwakarma, P., Tothadi, S., and Pratihar, S. (2023). Cooperative bimetallic Co−Mn catalyst: Exploiting metallo-organic and hydrogen bonded interactions for rechargeable C-/N-alkylation. ChemCatChem *15*, e202300828.

4. Khajevand, M., Azizian, S., and Jaleh, B. (2022). A bio-based 3D evaporator nanocomposite for highly efficient solar desalination. Sep. Purif. Technol. *284*, 120278.

5. Ding, N., Zhou, T., Weng, W., Lin, Z., Liu, S., Maitarad, P., Wang, C., and Guo, J. (2022). Multivariate synthetic strategy for improving crystallinity of zwitterionic squaraine-linked covalent organic frameworks with enhanced photothermal performance. Small *18*, 2201275.

6. Tian, P.J., Han, X.H., Qi, Q.Y., and Zhao, X. (2024). An azulene-based crystalline porous covalent organic framework for efficient photothermal conversion. Small *20*, 2307635.

7. Yan, X., Lyu, S., Xu, X.Q., Chen, W., Shang, P., Yang, Z., Zhang, G., Chen, W., Wang, Y., and Chen, L. (2022). Superhydrophilic 2D covalent organic frameworks as broadband absorbers for efficient solar steam generation. Angew. Chem. Int. Ed. *61*, e202201900.

8. Cui, W.R., Zhang, C.R., Liang, R.P., and Qiu, J.D. (2021). Covalent organic framework hydrogels for synergistic seawater desalination and uranium extraction. J. Mater. Chem. A *9*, 25611–25620.

9. Xia, M., Liang, Y., Luo, W., Cai, D., Zhao, P., Chen, F., Li, Y., Sui, Z., Shan, L., Fan, R., et al. (2022). 2D covalent organic framework-based core-shell structures for high-performance solar-driven steam generation. Mater. Today Energy *29*, 101135.

10. Cui, W.R., Zhang, C.R., Liang, R.P., Liu, J., and Qiu, J.D. (2021). Covalent organic framework sponges for efficient solar desalination and selective uranium recovery. ACS Appl. Mater. Interfaces *13*, 31561-31568.

11. Wang, F., Su, Y., Li, Y., Wei, D., Sun, H., Zhu, Z., Liang, W., and Li, A. (2020). Salt-resistant photothermal materials based on monolithic porous ionic polymers for efficient solar steam generation. ACS Appl. Energy Mater. *3*, 8746–8754.

12. Li, X., Pang, Y., Zhang, Y., Ge, B., Liu, J., Zhang, Y., Zhao, L., Ren, G., and Zhang, Z. (2023). Construction of covalent organic framework evaporator based on Bi/BiOCl floating layer and its application in solar desalination and clean water production. Sep. Purif. Technol. *326*, 124804.

13. Zhang, C.R., Cui, W.R., Niu, C.P., Yi, S.M., Liang, R.P., Qi, J.X., Chen, X.J., Jiang, W., Zhang, L., and Qiu, J.D. (2022). rGO-based covalent organic framework hydrogel for synergistically enhance uranium capture capacity through photothermal desalination. Chem. Eng. J. *428*, 131178.

14. Li, H.C., Li, H.N., Zou, L.Y., Li, Q., Chen, P.F., Quan, X.N., Deng, K., Sheng, C.Q., Ji, J., Fan, Q., et al. (2023). Vertically π-extended strong acceptor unit boosting near-infrared photothermal conversion of conjugated polymers toward highly efficient solar-driven water evaporation. J. Mater. Chem. A *11*, 2933–2946.

15. Yu, X., and Xuan, Y. (2018). Investigation on thermo-optical properties of CuO/Ag plasmonic nanofluids. Sol. Energy *160*, 200-207.

16. Seifikar, F., Azizian, S., Nasri, A., and Jaleh, B. (2023). Comparative study on photo-thermal conversion properties of vanadium nanofluids prepared by laser ablation in H_2O and polyethylene glycol. J. Ind. Eng. Chem. *123*, 72-80.

17. Shaker, M., Qin, Q., Zhaxi, D., Chen, X., Chen, K., Yang, S., Tian, H., and Cao, W. (2023). Improving the cold thermal energy storage performance of paraffin phase change material by compositing with graphite, expanded graphite, and graphene. J. Mater. Eng. Perform. *32*, 10275-10284.

18. Seifikar, F., Azizian, S., and Jaleh, B. (2024). Photo-thermal conversion ability of PEG and H $_2$O-based microfluids of sodium lignosulfonate and its carbonized form. Energy Adv. *3*, 1737-1745.

19. Seifikar, F., Azizian, S., Torabi, M., Zolfigol, M. A., and Yarie, M. (2023). Photo-thermal conversion properties of phosphonium-based ionic liquid, its magnetized and emulsion forms. Colloids Surf. A: Physicochem. Eng. Asp. *676*, 132249.

20. Seifikar, F., Azizian, S., Eslamipanah, M., and Jaleh, B. (2022). Efficient photo-thermal conversion using Pt nanofluid prepared by laser ablation in liquid. Sol. Energy Mater. *238*, 111581.

21. Seifikar, F., and Azizian, S. (2021). Super-stable carbon quantum dots nanofluid for efficient solar-thermal conversion. Energy Convers. Manage. *228*, 113675.

22. Luo, B., Han, Y., Yang, T., Li, J., Wang, H., Chen, W., and Li, X. (2021). Systematic investigating on the broadband solar absorption and photo-thermal conversion performance of TiN@rGO plasmonic nanofluids, Colloids and Surf. A Physicochem. Eng. Aspec. *630*, 127549.

23. Yan, Y., Li, Z. Y., Zhang, N. N., and Krautscheid, H. (2024). A π− π stacked porous framework for highly efficient second near-infrared photothermal effects and photo-thermo-electric conversion. Chem. Eng. J. *499*, 156059.

24. Yan, Y., Zhang, N. N., Si, J. W., Li, Z. Y., and Krautscheid, H. (2024). Bidirectional π- π stacking for near-infrared photothermal effects and photo-thermo-electric conversion in a semiconductive hydroxamate coordination polymer. Chem. Eng. J. *491*, 152054.

25. Huang, Q., Ye, X., Chen, W., Song, X., Chen, Y. T., Wen, X., Zhang, M., Wang, Y., Chen, S., Dang, L., and Li, M. D. (2023). Boosting photo-thermo-electric conversion via a donor–acceptor organic cocrystal strategy. ACS Energy Lett. *8*, 4179-4185.

26. Zhang, X., Cheng, P., Song, W., Rong, S., Huang, J., Wang, D., Schaaf, P., Zhou, G., Zhaang, Z., and Liu, J. (2022). Photo-thermoelectric conversion and photo-induced thermal imaging using 2D/3D ReS_2@ carbon framework with enhanced photon harvesting. Chem. Eng. J. *446*, 137084.

27. Zhang, X., Gao, W., Su, X., Wang, F., Liu, B., Wang, J. J., Liu, H., and Sang, Y. (2018). Conversion of solar power to chemical energy based on carbon nanoparticle modified photo-thermoelectric generator and electrochemical water splitting system. Nano Energy *48*, 481-488.

28. Geng, X., Zhang, D., Zheng, Z., Ye, G., Li, S., Tu, H., Wan, Y., Yang, P. (2021). Integrated multifunctional device based on Bi_2S_3/Pd: localized heat channeling for efficient photothermic vaporization and real-time health monitoring. Nano Energy *82*, 105700.

29. Zheng, Z., Li, H., Zhang, X., Jiang, H., Geng, X., Li, S., Tu, H., Cheng, X., Yang, P., Wan, Y. (2020). High-absorption solar steam device comprising Au@ Bi_2MoO_6-CDs: Extraordinary desalination and electricity generation. Nano Energy *68*, 104298.

30. Zhang, W. W., Guo, Y. M., He, M. J., Ren, Y. T., Gao, B. H., and Qi, H. (2024). Self-adaptive photothermal/radiative cooling-thermoelectric conversion system for 24 h electricity generation. Appl. Therm. Eng. *243*, 122603.

31. Amarnath, M., Basu, H., Basu, R., Chandwadkar, P., Acharya, C., Singh, S., Kailasa, S. K., and Patra, C. N. (2023). A Multifunctional tannic acid-Fe^{3+}-graphene oxide loaded alginate photothermal network: an interfacial water evaporator, a disinfector and a power generator. Mater. Adv. *4*, 4537-4554.

32. Karami, A., and Azizian, S. (2024). Fast and simple deposition of thin film of Cu_2-xS nanosheets on copper foil for solar energy harvesting via photo-thermo-electric conversion. Mater. Today Energy *41*, 101544.

33. Tahzibi, H., and Azizian, S. (2025). Considering micro/nanostructures at the surface of photothermal materials: A game changer in correct estimation of evaporation rate and energy conversion efficiency in interfacial solar vapor generation systems. Langmuir *41*, 999–1004.